Politecnico di Torino

Politecnico di Torino

Aerospace Engineering

A.a. 2025/2026

Graduation Session March/April 2026

Advanced traction system design for pressurized rovers for lunar surface exploration

Supervisors:

Giuseppe Palaia

Alfonso Pagani

Candidate:

Sofia Cova

Abstract

This thesis focuses on the conceptual design of a locomotion system for a lunar pressurized rover, as it represents the key subsystem enabling the mobility of the rover and the exploration of the lunar surface. Several wheel–soil interaction models, based on classical terramechanics, along with different wheel architectures, have been investigated in order to define a single, robust and efficient wheel configuration capable of operating on loose lunar regolith.

Assuming a rigid cylindrical wheel, the analysis starts from Bekker's semi-empirical pressure–sinkage relationship and the Mohr–Coulomb Failure Criterion, which are used to derive the vertical and longitudinal stress–strain relationships. The Jánosi–Hanamoto model is then introduced to describe shear deformation effects. These formulations are further extended using the Wong and Reece approach to account for the normal and tangential stress distributions along the wheel–soil contact interface. Subsequently, soil deformation models proposed by Yoshida and Ishigami are included to evaluate not only longitudinal traction performance but also lateral behavior.

Since closed-form expressions of the integrated stress distributions are not available, two approximation strategies are adopted to derive analytical expressions for the resulting forces and torques: firstly, a uniform stress distribution and, then, a quadratic stress distribution along the contact patch. The results of the study indicate that the former model tends to underestimate wheel performance. Wheel deflection effects are also considered. In the first model, deflection is introduced explicitly as a design variable, while in the second approach it is accounted for through the Substitute Circle method.

Four promising wheel architectures, compatible with the lunar environment and mission requirements, are selected for further analysis: the hoop spring wheel, the modified spiral spring wheel, the tweel wheel, and the twin-carcasses wheel. Starting from the selection of the contact elements with the ground, both analytical and numerical structural parametric models are developed and implemented in MATLAB and Patran–Nastran, respectively, to provide a preliminary design of the wheel.

The proposed methodology is extensible to a wide range of soft-soil terrains and can be generalized from rigid to flexible wheel configurations, making it suitable for broader planetary mobility applications.

Table of Contents

List of Tables

List of Figures

Chapter 1

Introduction

In recent years, the increasing interest in lunar exploration has led to the development of progressively more ambitious and innovative mission concepts. Among these, the pressurized rover represents a key enabling technology, designed to support human exploration over distances significantly exceeding those achieved during previous crewed lunar missions. Pressurized rover represent a fundamental element in the future of human space exploration, as they not only enable the establishment of potential long-term lunar bases and surface habitation, but also serve as essential testbeds for acquiring the operational experience and advanced technologies required for similar human exploration architectures on Mars.

This system works as a mobile habitat, providing a controlled and protected environment that includes life-support systems, crew accommodation for sleeping and eating and the infrastructure necessary to perform scientific research during extended surface operations.

Within this framework, the present study focuses on the locomotion system, which is responsible for defining the optimal traction, suspension, structural, propulsion and steering configuration of a lunar rover. Owing to the inherent complexity of this subsystem, the analysis is limited to the traction element, while preserving the possibility of future integration with suspension and propulsion models.

1.1 Scope

The purpose of this thesis is *to develop a parametric framework for identifying the optimal traction system configuration for lunar rovers, targeting high traction capability, low system mass and reduced energy consumption, while ensuring robust 'trafficability',which is the system ability to reliably traverse both soft soils and hard*

ground without loss of traction.

For the synthesis of wheeled rover configurations specifically tailored to long-duration lunar missions a practical framework has been formulated and implemented, starting from generic mission requirements and multiple design variables. Different combination are compared through performance metrics in order to highlight parametric trends and support trade-off analyses, leading to the selection of a suitable wheel concept for detailed design.

A key objective of this process is the identification of simplified relationships that enable the stress–strain behavior and the performances of the wheels to be represented within a purely analytical model. Only after this step, the set of optimal design variables is employed to evaluate, with a numerical model, the corresponding structural and mechanical characteristics, with particular emphasis on mass-related properties.

1.2 Approach

The methodology adopted to carry out this work consists of the following steps:

- Review of past planetary rovers and analysis of more recent locomotion system concepts applicable to lunar surface operations;
- Investigation of wheel physics and integration with terramechanics models for soft soil,based on linear and quadratic approximations. Introduction of wheel deformation effects.
- Sensitivity analysis of the main design parameters;
- Integration of the analytical and structural models and selection of an optimal configuration;
- Detailed parametric structural analysis at the wheel system architecture level.

A significant portion of this work is devoted to the identification and adaptation of terramechanics models of wheel–soil interaction suitable for quantifying the traction performance of wheeled rover configurations. The proposed framework is ultimately capable of relating geometric and physical attributes, trafficability performance and environmental and structural parameters, allowing for the simultaneous qualitative and quantitative evaluation of multiple candidate solutions and the associated design space. This approach enables a substantial reduction in preliminary design time for future developments. The derivation of the governing

configuration equations and their implementation are detailed throughout the thesis.

The structure of this work is organized as follows:

Chapter 2 presents an analysis of the lunar environment. It also reviews possible locomotion system architectures, both those previously employed in lunar missions and more recent concepts. Additionally, the physics of wheeled locomotion is introduced.

Chapter 3 focuses on terramechanics. A detailed analysis of wheel–soil interaction models is first presented, followed by the implementation of the final system of equations within the analytical framework. The chapter then examines the two approximations introduced into the integral model to enable its solution.

Chapter 4 focuses on the preliminary design process, starting from representative mission-driven requirements. A sensitivity analysis is first conducted to verify the expected behavior of the performance metrics as the design parameters vary. An analytical parametric study is then carried out to estimate local stress distributions and to determine forces, moments, torques and power requirements. This is followed by a numerical parametric study based on finite element methods, in which static analyses are used to evaluate mass properties, stress levels and structural displacements. The analytical and numerical models are subsequently integrated, ultimately leading to the selection of an optimal wheel configuration. Specifically, an investigation of the selected wheel architectures and the related manufacturing processes is done in order to identify the final wheel optimal type. The selected architecture is then examined in greater detail, with particular attention to how variations in thickness and reinforcement features influence its mechanical and structural characteristics.

Chapter 5 summarizes the main conclusions of the work and outlines potential directions for future developments.

Chapter 2

State of the Art

An important distinction must be made between the locomotion system and the traction system. The locomotion system can be defined as the ensemble of all subsystems that contribute to the overall mobility of the rover, including ground-contact elements, suspension systems, propulsion, actuation, steering mechanisms and the structural framework. The traction system, by contrast, specifically refers to the mechanism by which the driving force generated by the motor or propulsion unit is transmitted to the ground through the selected contact elements.

Before implementing an analytical model aimed at evaluating traction performance, it is, therefore, essential to select the ground-contact element on which the analysis is focused. Several options are considered, including wheels, tracked systems and mechanical legs, as well as more unconventional concepts such as hoppers and rolling balls. These alternatives are assessed based on their suitability for the mission objectives, manufacturing, assembly and maintenance complexity, safety and reliability considerations and key performance metrics such as low mass, reduced energy consumption and high traction capability.

Tracked systems and legged locomotion concepts present certain advantages in terms of terrain adaptability; however, they are generally associated with higher power consumption, increased frictional losses, mechanical inefficiencies and significant penalties in mass and maintenance complexity. Similarly, the other more exotic solutions, despite their conceptual appeal, suffer from limited technological maturity and pose challenges in terms of controll ability, reliability and system integration. As a result, these approaches are less suitable for long-duration lunar surface missions [1].

Following this trade-off analysis, wheeled locomotion emerged as the most suitable solution. Wheels offer a favorable combination of simplicity, ease of control,

high reliability, and technological maturity. In addition, wheeled systems satisfy fundamental mobility requirements on sandy, rocky or poorly characterized terrains, including bidirectional motion, steering capability, and obstacle negotiation. The integration of surface features such as grooves or grousers further enhances traction performance and the overall 'trafficability'.

2.1 Lunar environment

Before addressing the physics of wheel–soil interaction, it is essential to analyze the characteristics of the terrain with which the wheel comes into contact. The properties of the ground play a fundamental role in determining the optimal wheel design, as soil conditions directly influence traction performance, sinkage, and overall mobility. In this context, a comparison between the lunar and terrestrial environments is particularly relevant. Although wheels are intended to operate on the lunar surface (and may eventually be manufactured or assembled there) they are currently designed, built, and tested under terrestrial conditions, which differ significantly from those encountered on the Moon.

The majority of the lunar surface is covered by regolith, a fragmental and unconsolidated layer of material generated by continuous meteoritic impacts. This layer consists of fine dust, rock fragments, mineral grains, and glassy particles, with thickness typically ranging from approximately 5 to 15 meters. The primary elemental constituents of lunar regolith include oxygen, silicon, iron, calcium, aluminum and magnesium, along with various trace elements. Regolith overlies a compact substrate commonly referred to as bedrock and exhibits highly heterogeneous mechanical properties, even over relatively small spatial scales.

From a mobility standpoint, the friable and heterogeneous nature of regolith poses significant challenges for traction and load-bearing capability. While pneumatic tires have demonstrated excellent performance in terrestrial applications, they are fundamentally unsuitable for lunar conditions due to extreme temperature variations, vacuum operation, radiation exposure and mass and reliability constraints. As a result, non-pneumatic wheel concepts are required to ensure adaptability to surface irregularities, adequate traction on regolith and robust operation across a wide range of environmental conditions.

Beyond the characteristics of the soil itself, the lunar environment as a whole imposes additional constraints on wheel design. The reduced gravitational acceleration, the near-total absence of atmosphere by terrestrial standards and extreme thermal variations represent critical factors that affect material behavior, structural

integrity and wheel–soil interaction mechanisms.[2]

Several environmental factors further complicate surface operations on the Moon. The vacuum environment makes human activity and maintenance operations particularly challenging; permanently shadowed craters, while of high scientific interest, can represent extremely hostile environments for both astronauts and instrumentation; and fine dust particles, often electrostatically charged, can adhere to surfaces and negatively affect both electronic and mechanical systems. These conditions collectively contribute to the complexity of designing reliable mobility systems for lunar surface exploration [3].

Special considerations for lunar wheel development therefore include strict limitations on transport mass and volume, exposure to extreme temperatures (approximately $-230\,^{\circ}\mathrm{C}$ to $130\,^{\circ}\mathrm{C}$), operation under intense solar radiation without atmospheric shielding, rolling and sliding contact with unweathered regolith and abrasive dust particles, functionality in hard vacuum and performance in a reduced-gravity environment. These constraints strongly influence material selection, structural design and wheel–soil interaction modeling approaches [4]. Table 2.1 summarizes the main environmental differences between the lunar and terrestrial environments and highlights their most relevant implications for rover design, mobility and subsystem reliability.

Parameter	**Moon**	**Earth**	**Effect on Rover**
Atmosphere	Vacuum	Dense atmosphere	Lubricant evaporation, no convection, no pneumatic tires
Gravity	$\approx 1/6$ of Earth	$1g$	Lower traction and different wheel–soil interaction
Temperature	$+130^{\circ}\mathrm{C}$ to $-230^{\circ}\mathrm{C}$	Much milder range	Thermal stress on materials and electronics
Radiation	High solar and cosmic radiation	Naturally shielded	Damage to electronics and structures
Dust/Regolith	Fine, abrasive, electrostatic dust	Less abrasive soil/dust	Abrasion, adhesion, accumulation, sinkage

Table 2.1: Comparison between the main environmental characteristics of the Moon and the Earth, highlighting the main implications for rover design.

2.2 Wheel State of the Art

The wheel is one of the oldest and most transformative mechanical inventions in human history. Archaeological and historical studies commonly place the emergence of wheeled transport in the 4th millennium BC, marking a turning point in the relationship between mobility, load carrying and terrain negotiation. In this sense, ancient wheel remains are more than historical artifacts: they represent the beginning of a long technological trajectory in which the wheel progressively evolved from a simple enabler of terrestrial transport into a highly engineered subsystem for extreme environments. This perspective is especially useful when discussing planetary mobility, where the wheel is no longer a passive component, but a primary element governing locomotion, safety, energy efficiency and mission capability.

Figure 2.1: Ancient bronze wheel assembly - Lugdunum Museum and Roman Theatres in Lyon. The image is used here as a visual link between the earliest history of wheeled transport and the modern evolution of non-pneumatic wheels for planetary and pressurized rovers.

While the physical principle of rolling remains unchanged, the design requirements associated with wheels have dramatically expanded over time. In early terrestrial

applications, wheels were primarily required to support weight and reduce the resistance associated with dragging. In modern off-road and planetary systems, by contrast, wheels must also ensure traction on deformable soil, limit sinkage, tolerate impacts, absorb vibration, survive abrasive environments and maintain functionality under strict mass and reliability constraints.

This evolution becomes particularly evident in the field of space exploration. Planetary rovers do not operate on paved roads or even on conventional off-road terrain: they move over regolith, rocks, craters, slopes and highly heterogeneous surfaces, often in vacuum, under severe thermal cycling and with limited possibilities for maintenance or repair. As a result, the wheel has become a multifunctional engineering component at the intersection of terramechanics, structural mechanics, materials science and vehicle systems design. In the rover literature, wheel performance is therefore typically evaluated not only in terms of geometry and strength, but also through mobility metrics such as slip ratio, drawbar pull, rolling resistance, sinkage, contact patch evolution, obstacle surmounting capability and durability under cyclic loading.

A major milestone in this evolution was represented by the wheels developed for the Apollo Lunar Roving Vehicle (LRV). These non-pneumatic wheels employed a compliant wire-mesh structure with chevrons or tread elements designed to improve flotation and traction on lunar soil while keeping mass extremely low. Their design demonstrated that, in extraterrestrial applications, pneumatic tires are not necessarily the optimal solution. Instead, lightweight and compliant non-pneumatic architectures can provide a superior compromise between structural efficiency, terrain adaptability and operational robustness.

Subsequent studies have shown, however, that the Apollo solution cannot simply be scaled to future missions. Upcoming lunar and martian exploration scenarios involve heavier vehicles, longer traverses, higher duty cycles and more demanding operational tasks. These requirements are even more critical in the case of pressurized rovers, which must transport crew, life-support systems, scientific payloads and sometimes cargo over long distances while preserving ride quality, structural integrity and mission safety [5].

For this reason, recent research has increasingly focused on advanced non-pneumatic concepts such as mesh wheels, spring wheels, compliant metallic wheels, and shape-memory-alloy-based superelastic tires, with grousers. Compared with conventional pneumatic tires, these architectures eliminate the risk of puncture and can be tailored to achieve low local stiffness for terrain conformability together with high global stiffness for load support. More broadly, they reflect a shift in design philosophy: from the wheel as a rigid rolling element to the wheel as an adaptive interface between vehicle and terrain [4].

Within this framework, the historical development of the wheel can be interpreted as a progressive increase in functional integration. Ancient wheels enabled transport; industrial wheels improved speed, comfort and manufacturability; planetary wheels added compliance, lightweight construction and terrain-specific traction; and rover wheels for future pressurized missions are now expected to integrate locomotion, suspension-like behavior, structural resilience and, in some concepts, even actuation at the wheel level.

Terminology note

In this work, the terms *wheel* and *tire* are occasionally used interchangeably for the sake of readability and consistency with part of the rover-mobility literature. Strictly speaking, the two terms are not fully equivalent, since *tire* more properly refers to the outer compliant element in contact with the ground, whereas *wheel* may denote the broader load-bearing and rolling assembly. However, in the context of planetary rover studies, this distinction is not always maintained consistently and the present thesis follows this common usage whenever no ambiguity arises.

2.3 Wheel Phisics

In locomotion mechanics, at the initial stage, the vehicle dynamics are studied by modeling the system as a material point (Figure 2.2).

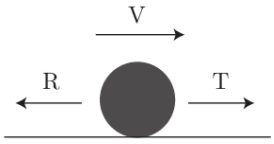

Figure 2.2: Traction model of a material point.

From this assumption, the general equation of motion of an isolated vehicle can be derived as

$$T - R = M_e \frac{dv}{dt} \tag{2.1}$$

where:

T = sum of all tractive forces,

R = sum of all resistive forces,

M_e = equivalent mass of the vehicle,

$\frac{dv}{dt}$ = vehicle acceleration.

As a wheeled rover, the vehicle operates under natural adhesion, with traction transmitted to the ground through rolling elements, namely the wheels, which are all driving wheels. The rover therefore adopts an all-wheel-drive traction system, which is particularly suited to pressurized rovers, as it must overcome surface irregularities while supporting significantly higher payloads than unpressurized ones.

On each driving wheel, in addition to the gravitational force and the sum of motion resistances, a driving torque transmitted through the motor shaft is applied. This torque directly influences the magnitude of the traction force (T). Depending on the balance between the applied driving torque, the adhesion force or friction resistance (A) and the resisting forces (R), different operating conditions may arise. These conditions are summarized in Table 2.2. (v is the longitudinal velocity).

$T < R$	$v = 0$	$T \leq A$	no motion of C and the wheel
		$T > A$	pure slip (without forward motion)
	$v \neq 0$	$T \leq A$	C coincides with CIR and wheel decelerate until it stops
		$T > A$	pure slip (without forward motion)
$T = R$	$v = 0$	$T \leq A$	no motion of C and the wheel
		$T > A$	pure slip (without forward motion)
	$v \neq 0$	$T \leq A$	C coincides with CIR and wheel moves forward rolling with constant velocity (rolling)
		$T > A$	slip, but wheel move forward with constant velocity
$T > R$	$v = 0$	$T \leq A$	wheel starts rolling
		$T > A$	pure slip (without forward motion)
	$v \neq 0$	$T \leq A$	C coincides with CIR and wheel moves forward rolling with increasing velocity (rolling)
		$T > A$	slip, but wheel move forward

Table 2.2: Operating conditions of a driving wheel.

For a driving wheel (characterized by an angular velocity $\omega \neq 0$), rolling motion, defined as the simultaneous occurrence of rotation and translation, can be achieved

only if specific conditions are satisfied:

$$R \leq T \leq A$$

In particular, the traction force must be sufficient to overcome the resistive forces acting on the wheel, while remaining within the limits imposed by both longitudinal and lateral adhesion in order to avoid, respectively, slipping and skidding. In other words, in the longitudinal condition, rolling without slip is ensured only if the required adhesion coefficient remains lower than the available friction coefficient:

$$f_x \leq \ f_a$$

where f_x is the adhesion coefficient demanded by the traction conditions (T), and f_a is the maximum friction coefficient provided by the wheel–ground contact (A).

On rigid terrain, the adhesion coefficient f_x increases with wheel load, which induces greater wheel deformation and surface compaction, increasing the contact patch area, while it decreases with velocity.
If the contact patch area is on the order of a few cm^2, the wheel motion cannot be described as pure rolling. In fact, two distinct regions can be identified within the contact patch (Figure 2.3) :

- **Region 1**: microslip region, where reversible elastic deformations and irreversible micro-sliding effects lead to a peripheral velocity that is slightly greater than the translational velocity, during traction (0<s<1)

$$\omega r > v.$$

- **Region 2**: pure rolling region, characterized by a zero relative velocity between the wheel and the ground (s=0)

$$v = \omega r.$$

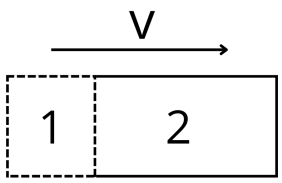

Figure 2.3: Regions of a cylindrical wheel Contact Patch.

Slip, or longitudinal sliding, can therefore be defined through the slip ratio

$$s = \frac{\omega r - v}{\omega r}$$

or, equivalently,

$$s = \frac{n\,2\pi r - L}{n\,2\pi r}.$$

where n is the number of wheel revolutions, r is the effective rolling radius, and L is the actual distance traveled by the wheel center.

- If $s = 0$ Pure Rolling
- If $s = 1$ Pure Slipping

[6]

Chapter 3

Terramechanics

Terramechanics is the engineering field that studies the soil properties and the interaction between wheeled or tracked vehicles and deformable terrain. A detailed assessment of the trafficability characteristics of the locomotion configurations is carried out by adopting quasi-static terramechanics models. The applicability of these models relies on the assumption that conventional ground vehicles and wheeled lunar rovers are subject to the same fundamental physical principles governing the interaction between locomotion elements and the terrain. The key difference lies in the fact that lunar locomotion occurs on a deformable and weakly constrained granular material, exhibiting low cohesion and limited load-bearing capability.

The following two problems must be overcome in conventional terramechanics simulations: (i) technical issues related to terrain surface modeling and (ii) limitations of terramechanics models themselves.

3.1 Terrain surface modeling

The first issue concerns terrain surface modeling, as an accurate evaluation of terrain surface characteristics is essential for lunar and planetary exploration. Prior to performing terramechanics analyses, a representative terrain field must be generated; however, methods for creating such terrain fields have not been extensively investigated. In real off-road environments, terrain geometry and soil properties vary significantly depending on the formation processes, and these variations should be properly reflected in terrain field simulations. In particular, on the Moon, soil parameters can change from one location to another as the vehicle traverses different terrains [2].

Table 3.1: Typical Lunar Soil Parameters

Symbol	Description	Value
n	Exponent of sinkage	1.0
k_c	Cohesive modulus of soil deformation	1,400 N/m^2
k_ϕ	Frictional modulus of soil deformation	820,000 N/m^3
ϕ	Coulombian angle of internal friction of soil	31.1 deg
c	Coulombian coefficient of cohesive strength of soil	170 N/m^2
γ	Soil weight density	2,470 N/m^3
K	Coefficient of soil slip	0.018 m
N_q	Terzaghi's bearing capacity friction factor	32.23
N_c	Terzaghi's bearing capacity cohesion factor	48.09
N_γ	Terzaghi's bearing capacity density factor	33.27
K_c	Cohesive modulus of soil deformation	33.37
K_γ	Density modulus of soil deformation	72.77

In this study, a conventional terramechanics analysis is adopted, in which the terrain properties are defined based on empirical knowledge and simplifying assumptions, such as homogeneous and flat surface conditions. [7] Accordingly, the regolith parameters are assumed to be constant and are specified in the simulation configuration file, as summarized in Table 3.1.

3.1.1 Internal friction angle

The value of the internal friction angle ϕ typically ranges between 30° and 40°. Therefore, the value corresponding to *loose sand* is selected, together with the empirical coefficients c_1 and c_2 reported in Table 3.2. These coefficients are empirically derived and are used to determine the relative position of the maximum radial stress of the wheel, θ_m, which is required for the computation of the maximum sinkage in Eq. (3.12), as described in [8].

Table 3.2: Typical values of terrain parameters for loose sand

Terrain Type	Angle of Internal Friction ϕ [deg]	c_1	c_2
Loose Sand	31.1	0.18	0.32

3.1.2 Shear deformation modulus

The parameter K, also referred to as the *shear deformation modulus*, which is the magnitude of the shear displacement required to develop the maximum shear stress, has been extensively investigated by Yoshida and Ishigami for different types of planetary terrains [9]. In the present work, the terrain is assumed to be homogeneous and isotropic, representative of lunar regolith. Under this assumption, the shear deformation modulus is identical in both the direction parallel to the motion (x) and the transverse direction (y), i.e. $K_x = K_y = K$, as also assumed in [10].

3.1.3 Soil bearing capacity

The bearing capacity is defined as the ability of the underlying soil to support applied loads without undergoing shear failure, and it is a concept traditionally associated with building and foundation engineering [11]. The soil bearing capacity can be evaluated using Terzaghi's bearing capacity theory. Although a wheel is not a foundation in a strict sense, the contact between a cylindrical wheel and a deformable soil can be modelled as an equivalent shallow *strip footing* problem. In this analogy, the vertical load W acting on the wheel is transmitted to the terrain through a finite contact patch, which can be approximated as a rectangular strip with width equal to the wheel width b and length l along the rolling direction, resulting in an equivalent contact area $A \approx b\,l$. Since the load is applied over a shallow region and induces a shear failure mechanism comparable to that of a surface footing, classical bearing-capacity concepts can be adopted to describe the load-carrying capability and the sinkage behaviour of the wheel.

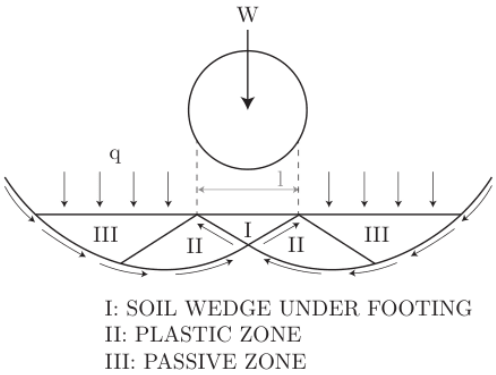

Figure 3.1: Equivalent shallow foundation analogy for a cylindrical wheel on deformable soil according to Terzaghi's bearing capacity theory.

In this framework (Figure 3.1), the vertical load W is resisted by shear stresses developing along the boundaries of three distinct failure zones beneath the footing, together with the contribution of the overburden pressure q acting above it [12]. The bearing capacity expression is composed of three main contributions: the first term accounts for the soil cohesion, the second term represents the effect of the footing embedment depth and the corresponding overburden pressure, while the third term is associated with the footing width and the extent of the shear failure zone.
The bearing capacity factors N_c, N_q, and N_γ are the classical Terzaghi bearing capacity factors and depend solely on the soil internal friction angle ϕ. These factors are defined as follows:

$$N_q = \frac{\exp\left[\left(\frac{3\pi}{2} - \phi\right)\tan\phi\right]}{2\cos^2\left(\frac{\pi}{4} + \frac{\phi}{2}\right)} \tag{3.1}$$

$$N_c = \frac{N_q - 1}{\tan\phi} \tag{3.2}$$

$$N_\gamma = \frac{2\,(N_q + 1)\tan\phi}{1 + 0.4\sin(4\phi)} \tag{3.3}$$

This formulation provides a physically meaningful interpretation of the soil reaction beneath the wheel and represents the basis for modelling the wheel–soil interaction in soft terrains.
In the present analysis, the adopted values are directly taken from [2] for lunar soil; however, they could also be derived as functions of the soil internal friction angle, ϕ.

While Terzaghi's bearing capacity theory provides a fundamental framework to describe the load-carrying mechanism of soil under shallow foundations, its direct application to wheel–soil interaction is limited by the assumption of a rigid footing and uniform stress distribution.
To overcome these limitations and to explicitly account for the progressive sinkage of a wheel into deformable terrain, Bekker extended the bearing capacity concept by introducing a pressure–sinkage relationship specifically tailored for vehicle mobility applications (Eq. (3.4)).

In Bekker's formulation, the normal stress at the wheel–soil interface is related to the local sinkage through empirical soil parameters, allowing the soil reaction to be expressed as a continuous function of penetration depth. This approach preserves the physical interpretation of soil resistance as governed by bearing capacity and shear failure mechanisms, while enabling the modelling of distributed contact stresses and varying contact geometries typical of rolling wheels on soft soil.

3.2 Terramechanics models

The second issue concerns the characterization of the contact between the tire and the ground. Modeling approaches represent a fundamental tool for the design and optimization of wheels, especially when moving from simple cylindrical disks to more sophisticated systems with intricate tread patterns.

Historically, empirical models were the most widely used, as they are based on experimental data and empirically derived relationships. With the advancement of computational power, numerical models have more recently emerged as a viable and powerful alternative. The choice of the tire–ground modeling approach depends on the specific behavior that needs to be investigated. Therefore, in this thesis, both approaches are employed: the former is used to evaluate the wheel performance in terms of trafficability, while the latter is adopted to analyze different types of tire patterns in greater detail, focusing on stress distribution and deformability. In general, modeling approaches for tire–ground interaction can be divided into three main categories: classical terramechanics models, numerical models and empirical approaches. The latter rely on physical testing to capture specific and complex interaction phenomena. This last approach is not addressed in the present work [13].

Classical terramechanics relies on semi-empirical modeling, combining experimental data with theoretical principles. The main advantages of these models are their low computational cost, ease of implementation and the generality of the resulting relationships. Moreover, they can be readily applied to wheels equipped with grousers or lugs to improve traveling performance.
However, the range of geometries that can be analyzed is limited, and surface deformation effects due to wheel–terrain interaction are only partially accounted for. Conventional terramechanics models allow for object penetration into the terrain, with stresses evaluated as a function of the intrusion depth. In practice, however, terrain deformation is more complex and involves not only compression but also material displacement.
For instance, in the Wong–Reece model (subsection 3.2.4), terrain deformation behind the wheel is represented in a simplified manner and only compressive deformation is considered, while the effects of soil being pushed forward or backward by the wheel are neglected [7].

The foundation of terrain-vehicle system relies on semi-empirical methods to obtain vertical and horizontal stress-strain relationship. From these relationship sinkage, forces and moments can be approximated. In Figure 3.2 there is a map of the forces and moments in order to specify the adopted sign conventions.

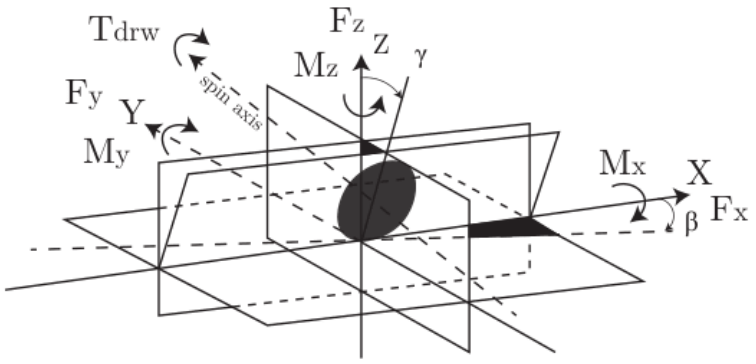

Figure 3.2: Map of forces and moments that act on the wheel.

In Figure 3.3 a logical flow of the classic terramechanics model is shown.

3.2.1 Bevameter

Both the plate-sinkage and annular shear tests are performed using a single testing device known as the bevameter (short for Bekker-Value-Meter), originally developed by M. G. Bekker (1950).

In the plate-sinkage test, a circular or rectangular plate, representative of the tire contact patch, is pressed vertically (W) into the terrain at a constant penetration rate. The measured force and corresponding sinkage (h) are used to characterize the vertical stress–strain ($\sigma(h)$) behavior of the soil (Figure 3.4).
In the annular shear test, a ring-shaped tool applies a normal load comparable to that experienced by a wheel and rotates on the terrain surface at a constant rate. The resulting torque–displacement response is then used to derive the horizontal stress–strain (τ) relationship (Figure 3.5).

3.2.2 Vertical stress-strain relationship

The vertical stress–strain relationship, also referred to as the pressure–sinkage relationship, reached its most established and widely accepted formulation with Bekker. The general concept underlying his theory is that the normal stress beneath a wheel at a given depth is equivalent to that obtained in a plate-sinkage test at the same depth.

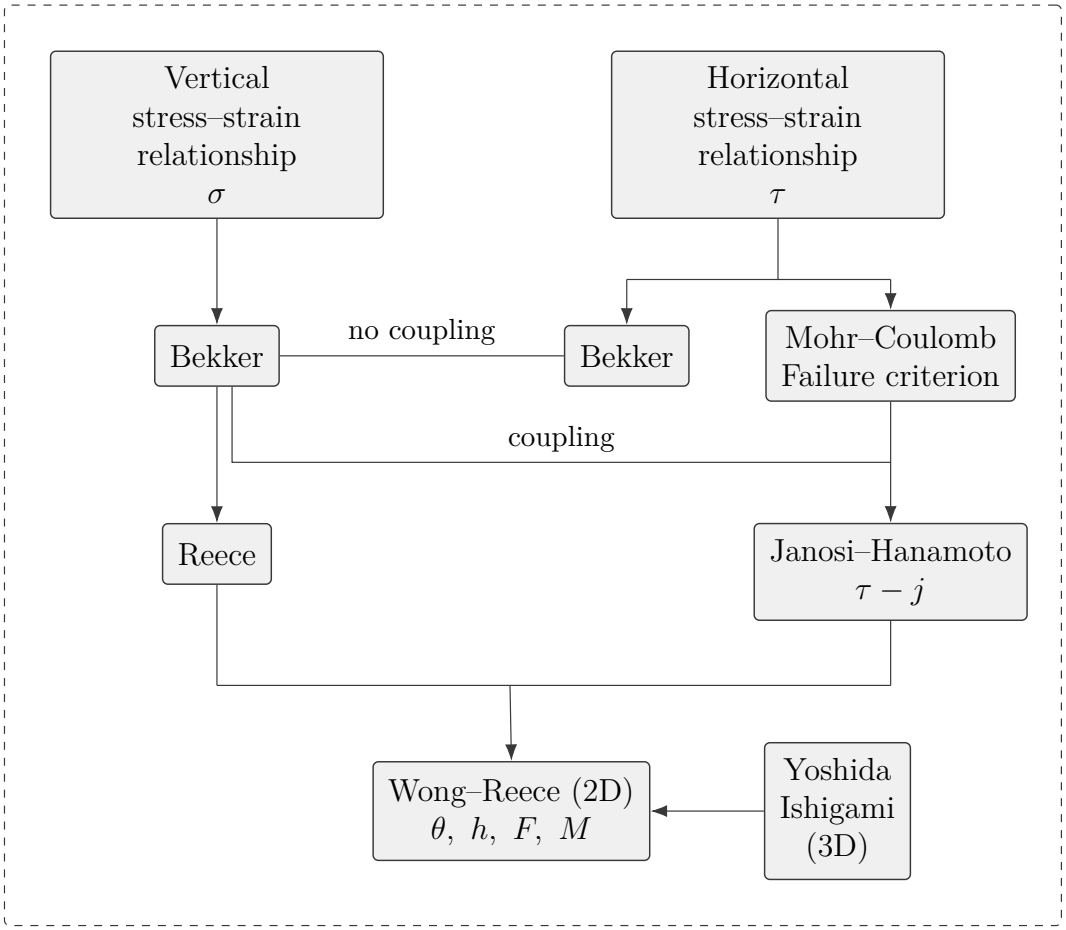

Figure 3.3: Conceptual map of classical terramechanics models.

$$\sigma(h) = \left(\frac{k_c}{b} + k_\phi\right) h^n \tag{3.4}$$

Here, σ is the pressure and normal stess, b is the width of the rectangular contact patch, h is the sinkage, and n, k_c, and k_ϕ are pressure-sinkage related parameters. These parameters are obtained from field tests conducted with the bevameter.
A development of Bekker was proposed by Reece, with the intent of giving more physics insight to the pressure sinkage dependency.

$$\sigma = \left(ck'_c + b\gamma_s k'_\phi\right)\left(\frac{h}{b}\right)^n \tag{3.5}$$

The Reece equation is extremely similar to Bekker's but it has the advantage to adopt purely dimensionless constants and normalized sinkage for different plate sinkage.

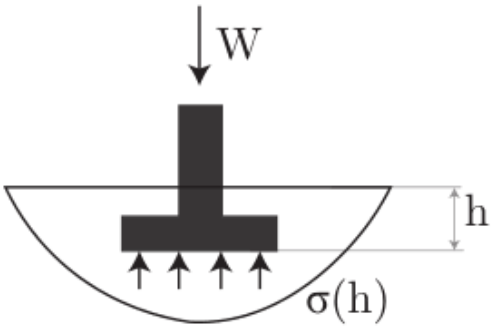

Figure 3.4: Plate-sinkage test.

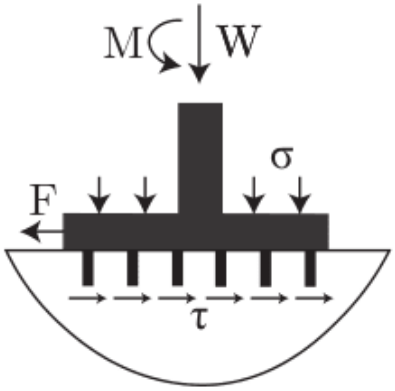

Figure 3.5: Plate-Shear test.

3.2.3 Horizontal stress-strain relationship

Bekker also proposed a relation to characterize the shear strength of the soil; however, in this formulation, no phisical coupling between shear displacement (kinematics) and normal stress is considered. The most commonly adopted formulation is based on the Mohr-Coulomb soil failure criterion. The maximum shear strength

of the soil is :

$$\tau_{\max}(\sigma) = c + \sigma \tan \phi \tag{3.6}$$

Here, c is the apparent cohesion, σ is the normal stress, and ϕ is the angle of internal shearing resistance of the material. These parameters can be derived from shear tests.
Than, Janosi and Hanamoto (1961) developed the horizontal stress-strain relationship, also known as the shear stress-shear displacement relationship. By combining the Mohr-Coulomb Failure criterion and the normal stress distribution, they predicted the shear stress. Specifically, an exponential function in addition to a new constant, the shear modulus, is employed for describing the shear stress-shear displacement relationship. Therefore, this equation is used to determine the amount of traction that a wheel will generate and how easily it will progress through terrain and surmount obstacles when driven.

$$\tau = (c + \sigma \tan \phi) \left(1 - e^{-\frac{j}{k}}\right) \tag{3.7}$$

Here, j is the shear displacement and K is the shear deformation modulus of the soil.

3.2.4 Bekker-Wong-Reece model

A significant step forward was the semi-empirical model proposed by Wong and Reece for rigid wheels on soft terrain, based upon Bekker's vertical stress-strain relation and Janosi-Hanamoto's horizontal stress-strain relation. The stresses were integrated along wheel-terrain interface (contact patch) in order to derive the sinkage, forces and torques acting on the wheel. It consists in a two-dimensional model, because lateral dynamics in not investigated (Figure. 3.6).

$$\sigma(\theta) = \left(ck_c^{'} + b\gamma_s \; k_\phi^{'}\right) \left(\frac{h(\theta)}{b}\right)^n \tag{3.8}$$

Where, the normal stress $\sigma(\theta)$ varies with the contact angle θ.

The sinkage as function of θ is expressed in:

$$h(\theta) = \begin{cases} r\left(\cos\theta - \cos\theta_f\right), & \theta_m \leq \theta \leq \theta_f, \\ r\left[\cos\left(\theta_f - \dfrac{\theta - \theta_r}{\theta_m - \theta_r}\left(\theta_f - \theta_m\right)\right) - \cos\theta_f\right], & \theta_r \leq \theta < \theta_m. \end{cases} \tag{3.9}$$

Here, r is the wheel radius. Furthermore, θ_f and θ_r are the entry and exit angles, respectively, which are calculated from the positional relationship between the

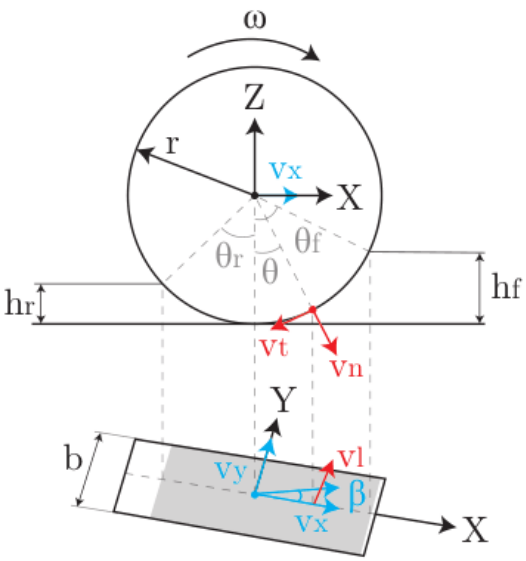

Figure 3.6: Wheel-soil contact geometry

wheel and the terrain surface. Moreover, θ_m represents the angle at the point of maximum normal stress $\sigma(\theta)$.

$$\theta_f = \cos^{-1}\left(1 - \frac{h_f}{r}\right) \tag{3.10}$$

$$\theta_r = \cos^{-1}\left(1 - \frac{h_r}{r}\right) \tag{3.11}$$

$$\theta_m = (c_1 + c_2 s)\,\theta_f \tag{3.12}$$

Here, h_f is the maximum sinkage; h_r is the elastic sinkage; c_1 and c_2 are referred to as the maximum stress angle constants and depend on the ground properties; s is the slip ratio.

Eq. (3.12) by Wong et Al. shows that the maximum of the pressure distribution occurs approximately halfway between the entry and exit angles and depends on the slip ratio. This fact was demonstrated by experimental evidence and the theory of plastic equilibrium, as reported from [10]. Although the sinkage increases monotonically from the entry angle to the bottom of the wheel, the corresponding stress distribution does not follow the same trend.

The tangential shear rate, the lateral shear rate and the compression speed corresponding to any contact angle θ can be derived as

$$v_t(\theta) = -v_x \cos\theta + r\omega \tag{3.13}$$
$$v_l(\theta) = v_y \tag{3.14}$$
$$v_n(\theta) = v_x \sin\theta \tag{3.15}$$

The shear stress τ generated in the tangential direction of the wheel is expressed by the equation Eq. (3.7) using the shear strength of the soil and the relative slip displacement j_t between the wheel and the soil, as function of θ:

$$\tau_t(\theta) = (c + \sigma(\theta)\tan\phi)\left(1 - \exp\left(-\frac{|j_t(\theta)|}{k}\right)\right) \tag{3.16}$$

Here, j_t is obtained by using a quasi-static approach: integrating the relative slip velocity v_t of the wheel surface over time (assuming that the velocity of terrain particles at the interface matches the velocity of the tire):

$$\begin{aligned} j_t(\theta) &= \int_0^t v_t \, dt \\ &= \int_{-\theta_r}^{\theta_f} \frac{r\omega\left[1 - (1-s)\cos\theta\right]}{\omega} \, d\theta \\ &= r\left[\theta_f - \theta - (1-s)\left(\sin\theta_f - \sin\theta\right)\right] \end{aligned} \tag{3.17}$$

Apparently, until this point, the models are purely 2D, thus only the longitudinal and the vertical stress can be calculated. Subsequently, the steering characteristics have been examined from Yoshida and Ishigami [14]. In particular, the soil deformation in the lateral (l) direction has been established in a similar way to the deformation in the longitudinal (t) direction.

$$\tau_l(\theta) = (c + \sigma(\theta)\tan\phi)\left(1 - \exp\left(-\frac{|j_l(\theta)|}{k}\right)\right) \tag{3.18}$$

$$j_l = \int_0^t v_l \, dt = \int_\theta^{\theta_f} v_x \sin\beta \, \frac{1}{\omega} \, d\theta \tag{3.19}$$
$$= \frac{v_x \sin\beta}{\omega}\left(\theta_f - \theta\right) \tag{3.20}$$
$$= r(1-s)(\theta_f - \theta)\tan\beta \tag{3.21}$$

Here, v_x is the traveling velocity of the wheel; β is the angle of lateral slip. When a vehicle is under the steering action, wheels side slip or skid.

$$\beta = \arctan(v_y/v_x) \tag{3.22}$$

In the top left part of Figure 3.7, a diagram of the forces (F_x = drawbar pull, W = wheel load), torque (T_{drw}) and stresses (τ = shear stress, σ = radial stress) acting on a rigid wheel driving over soft terrain (v_x = forward velocity of the wheel) is shown. The other diagrams show the stresses distribution.

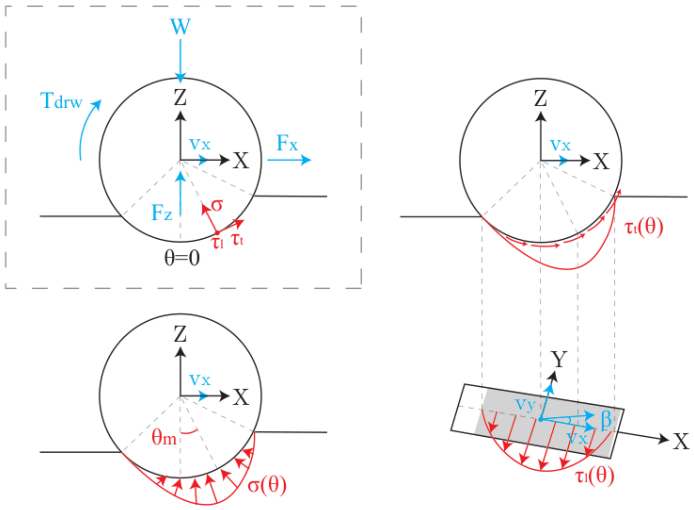

Figure 3.7: Normal and shear stresses along the contact area

3.2.5 Forces and torques

As anticipated in Subsection 2.3, traction is the force that produce relevant vehicle motion, developed when the wheels are powered. In this case a drive torque M_y is required to produce the tractive force F_T. The forces and torques acting on the wheel can be determined by integrating the stress along the wheel contact patch.

Longitudinal force:

$$F_x = br \int_{\theta_r}^{\theta_f} [\tau_t(\theta)\cos\theta - \sigma(\theta)\sin\theta]\, d\theta \tag{3.23}$$

F_x is the drawbar pull force (DP), which can also be written as the difference between the thrust force F_T and the compaction resistance force R_c. It is the force that is available to pull or push an additional payload until the maximum available traction is reached.

$$DP = F_x = F_T - R_c \tag{3.24}$$

$$F_T = br \int_{\theta_r}^{\theta_f} \tau_t(\theta) \cos\theta d\theta \tag{3.25}$$

$$R_c = br \int_{\theta_r}^{\theta_f} \sigma(\theta) \sin\theta d\theta \tag{3.26}$$

Lateral force:

$$F_y = -br \int_{\theta_r}^{\theta_f} \tau_l(\theta)\, d\theta - \left[\int_{\theta_r}^{\theta_f} R_b \left(r - h(\theta)\cos\theta\right) d\theta \right] \tag{3.27}$$

The analysis of steering is beyond the scope of this thesis; however, a brief discussion about the lateral forces is included for completeness. R_b is the lateral bulldozing resistance generated to unit width board of the wheel. This phenomenon was studied in different ways by Schwanghart [15] [10], based on the works of Hettiaratchi-Reece and Terzaghi, and by Yoshida and Ishigami, based on the Hegedus estimation [14] [9]. However both of them agreed about the evaluation of the lateral force by considering two contributions: the lateral shear stress developed at the wheel–soil contact patch and the bulldozing effect acting on the side face of the wheel. In the present work, only the lateral shear force is computed.

Vertical force:

$$F_z = br \int_{\theta_r}^{\theta_f} \left[\tau_t(\theta)\sin\theta + \sigma(\theta)\cos\theta\right] d\theta \tag{3.28}$$

Overturning moment:

$$M_x = -br^2 \int_{\theta_r}^{\theta_f} \tau_l(\theta)\cos\theta\, d\theta \tag{3.29}$$

M_y is the driving torque or rolling resistance moment:

$$M_y = -br^2 \int_{\theta_r}^{\theta_f} \tau_t(\theta)\, d\theta \tag{3.30}$$

Self-aligning moment:

$$M_z = -br^2 \int_{\theta_r}^{\theta_f} \tau_l(\theta)\sin\theta\, d\theta \tag{3.31}$$

The traveling efficiency indicates the efficiency at which the driving torque is converted into drawbar-pull.

$$\eta = \frac{F_x(1-s)\, r}{M_y} \tag{3.32}$$

3.2.6 Motion resistance

When a vehicle moves over a surface, it expends energy to overcome the resistive forces that arise during motion. These resistances can be external, resulting from the interaction between the wheels and the terrain (rolling resistance or gravitational effects) or internal, originating from friction within the vehicle components.
For locomotion on off-road terrain, the primary mechanisms of energy loss are soil compaction, bulldozing and soil dragging induced by the wheels.

Soil compaction resistance

Loss of traction in soft terrain is primarily caused by soil compaction resistance. Compaction can be interpreted as the vertical work per unit length required to press a wheel into the ground to a given fraction of its maximum sinkage. Equation (3.26) is based on the simplified Bekker wheel sinkage model expressed in Equation (3.4).

Bulldozing resistance

Bulldozing resistance develops when a substantial mass of soil is displaced by a wheel. This phenomenon may act both in the lateral (see Subsection 3.2.5) and longitudinal directions; however, in the present study only the longitudinal bulldozing effect is considered, namely when the soil is pushed in front of the wheel and directly affects vehicle trafficability.

Bulldozing resistance is particularly evident for wide wheels operating on soft soils. It has been shown to cause a significant increase in the total motion resistance for sinkage values exceeding approximately 0.06 times the wheel diameter [16]. Moreover, bulldozing resistance increases rapidly with the increasing of the tire width.

Bulldozing resistance can be estimated by applying the bearing capacity theory of soils under different failure criteria. The formulation adopted in this work was derived by Akin [2].

$$R_b = \frac{b\sin(\alpha+\phi)}{2\sin\alpha\cos\phi}\left(2hcK_c + \gamma h^2 K_\gamma\right) + \frac{l_0^3\gamma}{3}\left[\left(\frac{\pi}{2}-\phi\right) + \tan\left(\frac{\pi}{4}+\frac{\phi}{2}\right)\right] \tag{3.33}$$

$$\alpha = \cos^{-1}\left(1-\frac{2h}{d}\right) \tag{3.34}$$

$$l_0 = h_f \tan^2\left(\frac{\pi}{4}-\frac{\phi}{2}\right) \tag{3.35}$$

$$K_c = (N_c - \tan\phi)\cos^2\phi \tag{3.36}$$

$$K_\gamma = \left(\frac{2N_\gamma}{\tan\phi} + 1\right)\cos^2\phi \tag{3.37}$$

Here, α is the angle of attack of the wheel on the soil, l_0 is the length of soil ruptured by compression, and K_c and K_γ are the cohesive and density deformation moduli of the soil, respectively.

Unlike the lateral bulldozing models, which require integration along the contact region, this formulation is expressed in closed form and provides the total bulldozing force already integrated over the wheel width.

Rolling resistance

The rolling resistance is caused by the deflection of the tire and the tread elements, wheel slip and scrubbing at the wheel-soil interface. When wheel slip and scrubbing are negligible, rolling resistance can be attributed solely to energy dissipation due to wheel deformation and can therefore be modeled as

$$R_r = f_r W_w \tag{3.38}$$

Here, W_w is the vertical load applied on the wheel and f_r is an experimental coefficient depending on travelling speed, wheel slip, tire material, design, temperature, loading and the type of soil.

Gravitational resistance

When vehicle is on an slope, the gravitational resistance can be modeled as

$$R_g = W_w \sin\theta_\mathrm{s} \tag{3.39}$$

Here, θ_s is the angle of slope (positive for uphill and negative for downhill).

There can be also another component of resistance. The obstacle resistance develops when a vehicle climbs an obstacle, which cause a variation of the weight over the wheels. Modeling this resistance in soft soils and compliant obstacles is a specific process that goes beyond the purposes of this thesis.

Drive torque and power

Defined all these longitudinal resistances, the drawbar pull can also be computed as difference of the traction force (eq 3.25) and the sum of all the resistances [16] [17].

The torque due to resistive forces is

$$T_{\text{drw}} = (R_c + R_b + R_r + R_g)\left(\frac{d}{2}\,\delta_w\right) \tag{3.40}$$

Here, d is the diameter and δ_w is the deflection of the wheel.

The equation expresses the torque required at the wheel to sustain traction. It therefore imposes a constraint on the design of the robot's actuation and drivetrain subsystems. It must be noted that the drive torque computed should not be used to determine the total torque required to the vehicle, but only the moment needed to the individual wheel.

Drive power is the power required to be transmitted to the output of the wheels to sustain traction.

$$P_{\text{drw}} = T_{\text{drw}}\left(\frac{2v_x}{d}\right) \tag{3.41}$$

3.2.7 Hypothesis and assumptions

It is important to emphasize that the formulations presented in this section are valid for rigid cylindrical wheels. A rigid wheel can be regarded as a first approximation of a flexible tire, particularly when the terrain stiffness is significantly lower than the tire stiffness.
Furthermore,the modeling approach relies on several simplifying assumptions.

- For a sinking wheel, the normal stress calculated at a given sinkage is assumed to act along the radial direction of the wheel rather than along the vertical z-direction.
- Tangential and lateral shear stress are derived based on the isotropic shear stress assumption: the shear stress at any point of the wheel-soil interface is always opposite to the shearing velocity at that point. It's a more accurate method than the anisotropic one.
- The tire–soil contact patch is approximated by a bevameter plate: while the actual tire contact area has a curved geometry, the bevameter is characterized by a flat contact surface.
- The terrain is assumed to be homogeneous and isotropic.

3.3 Closed-form approximations

The main limitation of the classical terramechanics integrals described above is that they cannot be solved analytically, since they involve complex stress distributions that are computationally heavy and time-consuming to evaluate.

To overcome this issue, two simplified closed-form wheel-soil interaction models are analyzed in order to improve the efficiency of performance prediction and to obtain a parametric formulation adaptable to different mission conditions.
The first model assumes a constant distribution of normal and shear stresses along the wheel-soil contact region. The second model is derived by introducing a quadratic approximation of the stress distribution along the wheel-soil interface.

The second more refined model is introduced to improve the accuracy of the results, since stress distributions are generally nonlinear. Constant or linearized models can typically be applied only to straight-line driving scenarios, as also suggested in [18]. Moreover, the constant-stress approximation becomes less accurate as the soil sinkage exponent n decreases. Therefore, in order to ensure applicability to a wider range of soft soils beyond lunar regolith, a more general and accurate formulation is required.

The two models will be compared in Section 4.2

3.3.1 Constant approximation

A closed-form solution consists in assuming a uniform distribution of normal pressure σ along the tread-soil interface and a uniform shear displacement j [16].

$$\sigma = \frac{W_w}{A_w} \tag{3.42}$$

$$j = sl_w \tag{3.43}$$

$$A_w = b_w l_w \tag{3.44}$$

Here, A_w, b_w and l_w are respectively the area, width and the length of the rectangular contact patch.
The value of l_w is derived from geometric consideration, always assuming a rigid wheel, while for b_w is assumed equal to the width of the tire.

$$l_w = \sqrt{h_f(2r - h_f)} + \sqrt{h_r(2r - h_r)} \tag{3.45}$$

Here, h_f and h_r are the sinkages of the terrain corresponding respectively to the entry and exit contact angle. If $|\theta_f| = |\theta_r|$, $h_f = h_r = h$.

The shear stress can therefore be computed using the Janosi–Hanamoto law (Eq. 3.7) by substituting the previously obtained normal stress. Finally, the traction force is derived by integrating the shear stress over the entire contact patch.

$$F_T = \int \tau \, dA \tag{3.46}$$

$$F_T = A_w(c + \sigma \tan\phi)\left(1 - e^{-j/K}\right) \tag{3.47}$$

The drawbar pull is calculated using Eq. 3.24, with the compression resistance of a wheel on soil derived from Akin and based on the nonlinear spring soil model [2].

$$R_c = (k_c + k_\phi b)\frac{h^{n+1}}{n+1} \tag{3.48}$$

$$h_f = \left(\frac{3}{3-n}\frac{W}{(k_c + bk_\phi)\sqrt{d}}\right)^{\frac{2}{2n+1}} \tag{3.49}$$

$$R_c = \frac{1}{n+1}\left(\frac{3}{3-n}\frac{W}{\sqrt{d}}\right)^{\frac{2(n+1)}{2n+1}}\left(\frac{1}{k_c + bk_\phi}\right)^{\frac{1}{2n+1}} \tag{3.50}$$

3.3.2 Quadratic approximation

A closed-form solution of Eqs. 3.23, 3.27, 3.28, 3.29, 3.30, 3.31 can be obtained if the stress distribution is expressed as polynomials of θ. In particular, this approach is referred to as the quadratic approximation method.
In order to compute the stress distribution, two additional angles are introduced: the front medium angle θ_{fm} and the rear medium angle θ_{rm}.

$$\theta_{fm} = \frac{\theta_f + \theta_r}{2}, \qquad \theta_{rm} = \frac{\theta_r + \theta_m}{2} \tag{3.51}$$

The quadratic form of the stresses is derived as

$$\tilde{p}(\theta) = a_i^p\theta^2 + b_i^p\theta + c_i^p \qquad \left(\theta_i^l \le \theta \le \theta_i^u\right) \tag{3.52}$$

with

$$\begin{bmatrix} a_i^p \\ b_i^p \\ c_i^p \end{bmatrix} = \begin{bmatrix} \theta_m^2 & \theta_m & 1 \\ \theta_{im}^2 & \theta_{im} & 1 \\ \theta_i^2 & \theta_i & 1 \end{bmatrix}^{-1} \begin{bmatrix} p_m \\ p_{im} \\ p_i \end{bmatrix} \tag{3.53}$$

Here,

$$i = f, r; \qquad p = \sigma,\ \tau_t,\ \tau_l; \qquad \theta_r^l = \theta_r,\ \theta_r^u = \theta_f^l = \theta_m,\ \theta_f^u = \theta_f.$$

The subscript i denotes the front or rear region, while the superscript p denotes the stress type.
Now, the closed-form expression of the forces and torques can be calculated by replacing the stresses in the integral equations.

$$\begin{cases} \tilde{F}_x = rb \sum\limits_{i=f,r} \begin{bmatrix} (a_i^{\tau_t}(\theta^2-2) - 2a_i^{\sigma}\theta + b_i^{\tau_t}\theta - b_i^{\sigma} + c_i^{\tau_t})s\theta & + \\ (a_i^{\sigma}(\theta^2-2) + 2a_i^{\tau_t}\theta + b_i^{\sigma}\theta + b_i^{\tau_t} + c_i^{\sigma})c\theta & \end{bmatrix}_{\theta={}^l\theta_i}^{\theta={}^u\theta_i} \\ \tilde{F}_y = -rb \sum\limits_{i=f,r} [a_i^{\tau_l}\theta^3/3 + b_i^{\tau_l}\theta^2/2 + c_i^{\tau_l}\theta]_{\theta={}^l\theta_i}^{\theta={}^u\theta_i} \\ \tilde{F}_z = rb \sum\limits_{i=f,r} \begin{bmatrix} (a_i^{\sigma}(\theta^2-2) + 2a_i^{\tau_t}\theta + b_i^{\sigma}\theta + b_i^{\tau_t} + c_i^{\sigma})s\theta & + \\ (-a_i^{\tau_t}(\theta^2-2) + 2a_i^{\sigma}\theta - b_i^{\tau_t}\theta + b_i^{\sigma} - c_i^{\tau_t})c\theta & \end{bmatrix}_{\theta={}^l\theta_i}^{\theta={}^u\theta_i} \end{cases}$$

$$\begin{cases} \tilde{M}_x = -r^2b \sum\limits_{i=f,r} \begin{bmatrix} a_i^{\tau_l}(\theta^2-2)s\theta + 2a_i^{\tau_l}\theta c\theta \\ + b_i^{\tau_l}\theta s\theta + b_i^{\tau_l}c\theta + c_i^{\tau_l}s\theta \end{bmatrix}_{\theta={}^l\theta_i}^{\theta={}^u\theta_i} \\ \tilde{M}_y = -r^2b \sum\limits_{i=f,r} [a_i^{\tau_t}\theta^3/3 + b_i^{\tau_t}\theta^2/2 + c_i^{\tau_t}\theta]_{\theta={}^l\theta_i}^{\theta={}^u\theta_i} \\ \tilde{M}_z = -r^2b \sum\limits_{i=f,r} \begin{bmatrix} -a_i^{\tau_l}(\theta^2-2)c\theta + 2a_i^{\tau_l}\theta s\theta \\ -b_i^{\tau_l}\theta c\theta + b_i^{\tau_l}s\theta - c_i^{\tau_l}c\theta \end{bmatrix}_{\theta={}^l\theta_i}^{\theta={}^u\theta_i} \end{cases}$$

3.3.3 Elastic wheel

The numerical analysis carried out as the second design step is based on the best performance obtained through the analytical parametric process. However, in order to introduce the mass of the wheel as a new metric and to evaluate how wheel deflection effectively influences the rover trafficability, the flexible wheel configuration is also included. Regardless, the wheel's elastic characteristics are assessed more realistically through FEM analysis.

In the first case (uniform stress distribution), wheel flexibility is accounted for by introducing the wheel deflection as a design variable and by computing an effective sinkage.

$$h_{\text{eff}} = h + \delta \tag{3.54}$$

Here, δ is the deflectionof the wheel. An iterative fixed-point scheme is then adopted to obtain a self-consistent contact patch length: at each iteration h_{eff} is used to update the contact area and the average pressure, from which the soil sinkage h is re-evaluated via the Bekker relation until convergence.

In the second case (quadratic stress distribution), the wheel deformability is modeled through the Substitution circle method [7], [9]. It should be noted that the deflection is no longer treated as a design variable; instead, it directly depends on the normal force acting on the wheel and on a constant wheel stiffness. This choice is made to simplify the computation, since iterative procedures must be performed within the parametric design loop.

The deformation of the flexible tire during traveling can be approximated as a rigid wheel having a larger radius of curvature than that of the wheel before deformation (Figure 3.8).

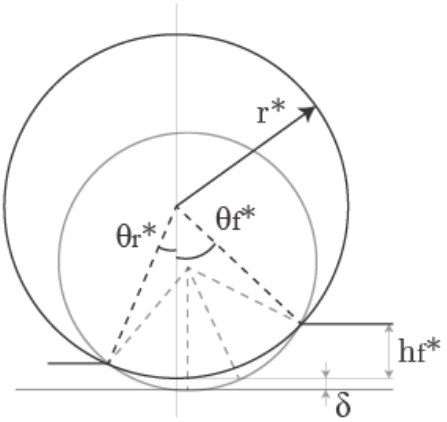

Figure 3.8: Substitution circle model for flexible tire.

The sinkage under the center of the flexible tire is h_f and the sinkage under the tire before deformation is h_f^*. The relationship between these quantities is:

$$h_f^* = h_f - \delta \tag{3.55}$$

The radius r^* of the substitution circle is derived from the following approximate expression, originally proposed by Bekker:

$$\sqrt{\frac{r^*}{r}} \approx \sqrt{1 + \frac{\delta}{h_f^*}} + \sqrt{\frac{\delta}{h_f^*}} \tag{3.56}$$

The forces of a flexible tire is obtained by evaluating the stress distribution using r^* and h_f^* in the same equation of the rigid tire.

Chapter 4

Preliminary design

This chapter describes the preliminary design approach adopted for the lunar rover locomotion subsystem, focusing on the study of cylindrical wheels.
The proposed methodology can be interpreted as a co-optimization framework for parametric design and wheel selection, where mobility performance, power consumption and structural characteristics are simultaneously evaluated across a wide range of design configurations and architectures through specific metrics.
This integrated analysis enables the identification and ranking of the most promising wheel within the explored design space, which constitutes the main objective of this thesis.

The methodological workflow adopted for the preliminary design of the cylindrical wheel is summarized in Fig. 4.1.

In the context of space systems, the preliminary design phase aims at translating mission requirements and operational constraints into a consistent set of design parameters and evaluating their impact on system performance through simplified but physically meaningful models.
The main configuration parameters of the rover wheel are varied systematically. These parameters include wheel diameter and width, number of wheels, rover mass, slip ratio and translational velocity. In parallel, the interaction between the wheel and the lunar regolith is modeled through a terramechanics-based approach, using soil parameters representative of soft lunar regolith conditions.
Two computational implementations of the terramechanics model have been developed in order to evaluate the robustness of the results and the influence of modeling assumptions. In particular, the stress distribution at the wheel–soil interface is approximated using uniform and quadratic stress distributions, allowing a comparison of the predicted traction performance under different modeling assumptions (See Chapter 3) .

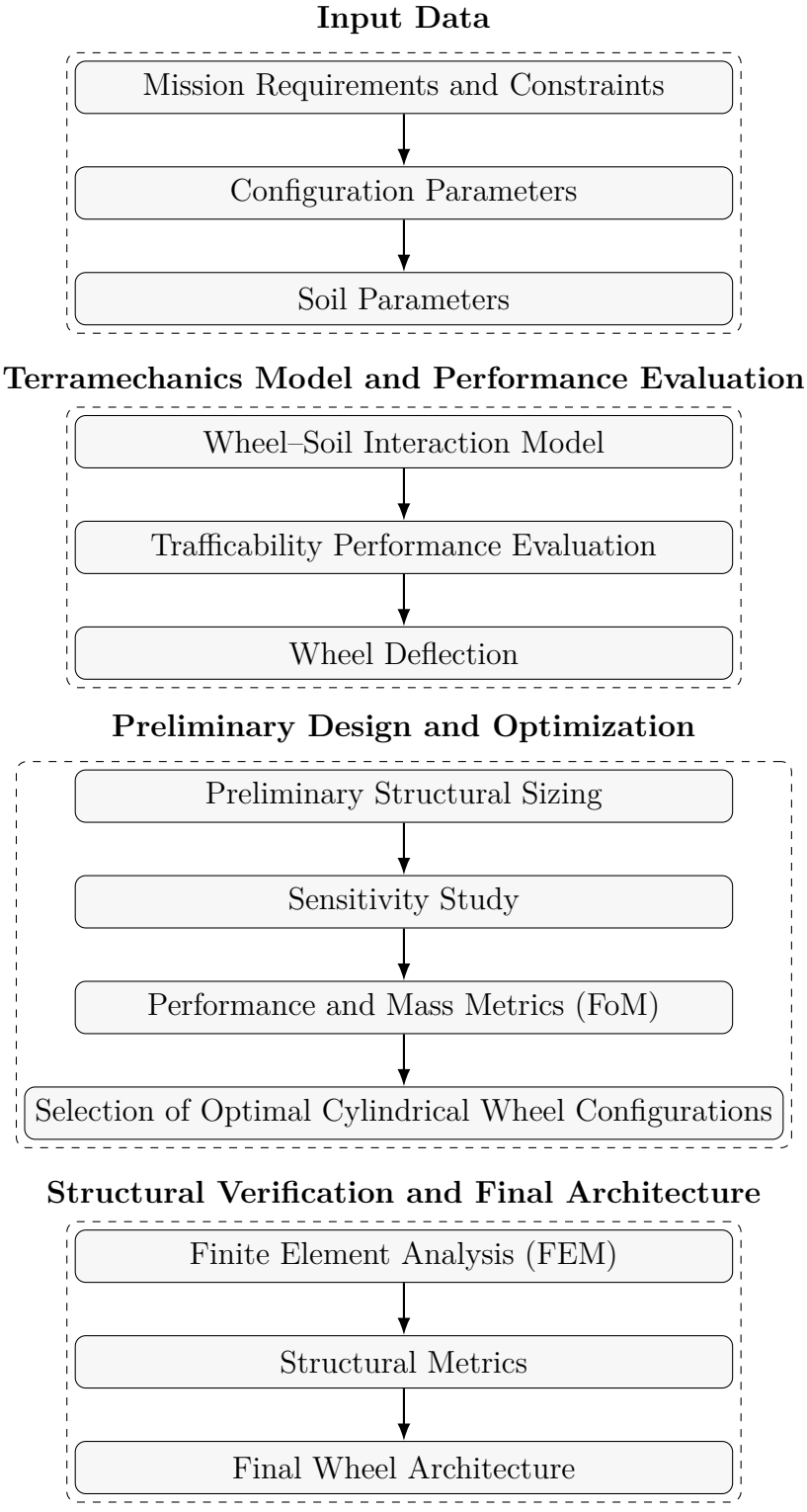

Figure 4.1: Workflow adopted for the preliminary design of the cylindrical wheel for a lunar rover.

For each combination of parameters, the model computes the wheel–soil contact geometry, including sinkage and contact angles. Based on these quantities, the main trafficability performance indicators are evaluated, including drawbar pull, motion resistances, required torque and drive power.

At the same time, a preliminary structural sizing of the wheel is performed by estimating the required thickness and resulting mass assuming an unique material, for simplicity (Aluminum). This allows the direct coupling between mobility performance and structural penalties, which is essential in the design of planetary exploration systems where mass is a critical driver.
The large number of simulated configurations enables a sensitivity analysis of the design variable, which allows a rapid exploration of the design spaces. Furthermore, it enables the definition of global performance metrics combining traction capability, power consumption and structural mass. These metrics are normalized and combined into a Figure of Merit (FoM) used to rank all configurations and select the candidate one for more detailed analyses.
The configurations with the highest FoM values are then selected as candidate cylindrical wheel architectures. These solutions are further investigated through finite element analyses (FEM) in order to obtain more accurate estimates of structural stiffness and mass. The results of this final step lead to the identification of the most suitable wheel architecture for the considered lunar rover application.

4.1 Requirements and constraints

4.1.1 Design space

In order to perform the preliminary design and the parametric exploration of the wheel configurations, a set of design requirements and bounds is defined for the main configuration variables. These limits do not represent strict mission requirements, but rather define a representative design space for pressurized lunar rovers operating on soft regolith terrain.
The main design variables considered in the present analysis include the wheel geometry, rover mass and configuration, and operational parameters related to vehicle motion.
The ranges adopted for the main design variables are summarized in Table 4.1.

The wheel geometry, represented by its diameter and width, plays a fundamental role in determining the interaction between the wheel and the lunar regolith. Variations in these parameters influence the contact area with the terrain, the resulting ground pressure and the sinkage behaviour on deformable soils. Larger contact areas generally reduce the average pressure exerted on the regolith and can improve

Table 4.1: Design variables and ranges adopted for the parametric study.

Parameter	Symbol	Range	Unit
Wheel diameter	d	0.6 – 2.0	m
Wheel width	b	0.4 – 0.8	m
Slip ratio	s	0.1 – 0.5	–
Vehicle velocity	v	0.1 – 8	m/s
Rover mass	m	1500 – 7000	kg
Number of wheels	N_w	4 – 10	–

trafficability, while at the same time introducing potential penalties in terms of structural mass and packaging constraints.

Operational parameters such as wheel slip and vehicle velocity are also considered in the analysis, as they directly influence the development of shear stresses at the wheel–soil interface and the energetic requirements of the locomotion system. In particular, wheel slip governs the generation of traction forces in terramechanics-based models and therefore represents a key parameter for evaluating rover mobility under different operating conditions.

The overall vehicle mass and the number of wheels define the load distribution acting on each wheel and therefore strongly affect the resulting wheel–soil interaction. Variations in these parameters allow the assessment of different rover architectures and their influence on trafficability performance, sinkage and traction capability when operating on soft lunar regolith.

4.1.2 Requirements

The mission statement of a pressurized lunar rover locomotion system can be summarized as the capability to support crew transportation and surface exploration activities by providing reliable mobility, adequate traction and load-carrying capability on the highly deformable and rugged terrain typical of the lunar surface for long distances.
Therefore the wheel design must satisfy several functional and structural requirements in order to operate effectively on soft soil (the following requirements are expressed in a generalized form and do not explicitly account for different terrain or path conditions. They instead represent structural and operational constraints that define the design space explored in the present analysis [17], [19]):

- The wheel shall be capable of transferring sufficient traction to the ground in

order to ensure rover mobility under nominal operating conditions.

- The motion resistances generated by the wheel–terrain interaction shall be minimized in order to reduce the required drive torque and power consumption.
- The wheel shall operate reliably in the lunar environment, including the absence of atmosphere and the presence of highly abrasive regolith.
- The wheel shall be mechanically integrated with the drive system and shall interface with the electric motor located within the wheel hub.
- The mass of the wheel shall be minimized in order to reduce the overall mass of the locomotion subsystem and improve system efficiency.
- The wheel tread shall be capable of sustaining the stresses generated by the wheel–terrain interaction without structural failure or excessive deformation.
- The wheel shall support the loads transmitted by the rover while maintaining structural integrity during operation on deformable terrain.
- The radial stiffness of the wheel should remain sufficiently uniform along the circumference in order to limit vertical oscillations of the rover chassis during motion.
- The wheel must maintain adequate axial and tangential stiffness to ensure stable and smooth behaviour during steering and maneuvering operations.

4.2 Sensitivity study

A sensitivity study evaluates how each design variable (Tab. 4.1) affects the outputs of the analysis, here the traction-system performance, while keeping all the others fixed.
This study is carried out using two different modelling approaches: a uniform approximation of the stress distribution and a quadratic approximation. In addition, both rigid and flexible wheel configurations are considered. The results show that the qualitative trends are very similar across the two models, and that, in general, the flexible wheel achieves better performance than the rigid wheel on soft terrain. For this sensitivity analysis, only maximum sinkage, drawbar pull, total motion resistance, and power consumption are plotted. However, as discussed in section 4.3, additional outputs, such as contact angles and stresses distribution, are also of interest and will be examined only for the flexible wheel with a quadratic stress distribution, which represents the most realistic case.

The analysis was carried out by fixing all the design variables except one, in order to evaluate how each parameter influences the system performance. The selected nominal values of the fixed parameters are reported in Table 4.2, while the ranges of the design variables are given in Table 4.1.

Parameter	**Symbol**	**Nominal value**	**Unit**
Wheel diameter	d	0.9	m
Wheel width	b	0.4	m
Slip ratio	s	0.2	–
Vehicle velocity	v	5	m/s
Rover mass	m	7000	kg
Number of wheels	N_w	6	–

Table 4.2: Nominal design parameters for wheel–terrain performance sensitivity analysis

Single-variable sensitivity analysis

The following section presents the plots and a discussion of the results obtained from the single-parameter analysis, with all other parameters held constant.

Wheel diameter is one of the main parameters affecting rover mobility on soft lunar regolith, as shown in Fig.4.2. As the wheel diameter increases, the maximum sinkage decreases. This is consistent with classical terramechanics: a larger wheel creates a longer contact area with the soil and reduces the average ground pressure, which improves terrain support. For the same reason, motion resistance also decreases, since compaction and bulldozing effects become less severe.
Because the resistance is lower, the drive power required at a given forward speed also decreases. At the same time, drawbar pull increases with the diameter, because traction is generated over a larger contact area while the resistive forces are reduced. The overall result is a larger traction margin and better mobility performance.

Wheel compliance provides an additional benefit on soft soil. An elastic wheel increases the effective contact area and reduces local pressure peaks, which leads to lower sinkage and lower motion resistance. As a consequence, drawbar pull improves while the required drive power decreases.

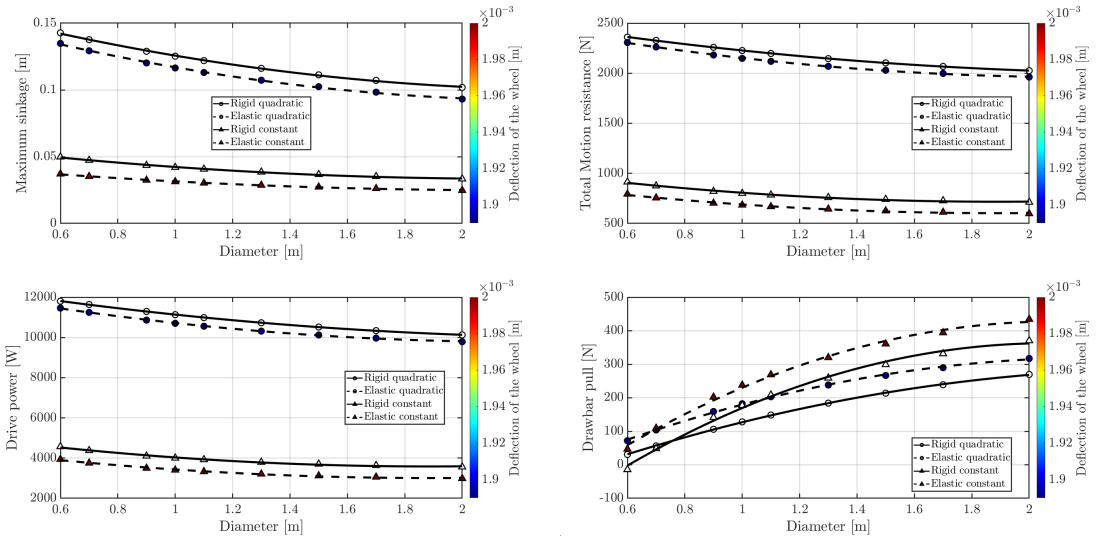

Figure 4.2: Comparison of two approximate models (quadratic and constant stress distributions) for rigid and elastic wheels. Top left: sinkage versus diameter; top right: resistance versus diameter; bottom left: drive power versus diameter; bottom right: drawbar pull versus diameter. The color bar highlights the effect of wheel deflection.

Finally, the uniform, cost-effective stress approximation shows the same general trends as the quadratic stress model, but it tends to predict slightly more optimistic performance. The observed differences in the results may be partly attributed to variations in wheel deflection; however, they are mainly due to the fact that the constant model is a much simpler approximation than the quadratic one. This simplification affects not only the stress distribution, but also the modeling of slip effects, as also evident in Fig.4.4. Moreover, the constant model does not take into account possible variations in the entry angle.

Fig. 4.3 reports the sensitivity to wheel width. Increasing b enlarges the contact patch area and reduces the average ground pressure, leading to a systematic decrease in maximum sinkage for both rigid and compliant wheels and for both modelling approximations. However, the total motion resistance shows a slight increasing trend with b. This response indicates that width-dependent resistive mechanisms (probably bulldozing contributions that scale with b) can outweigh the reduction in compaction-related losses associated with the lower sinkage.
Consequently, at fixed forward speed the drive power demand increases moderately with wheel width, reflecting the higher overall resistive force. The drawbar pull decreases with b, since the growth in resistive losses is not compensated by a proportional increase in traction capability.

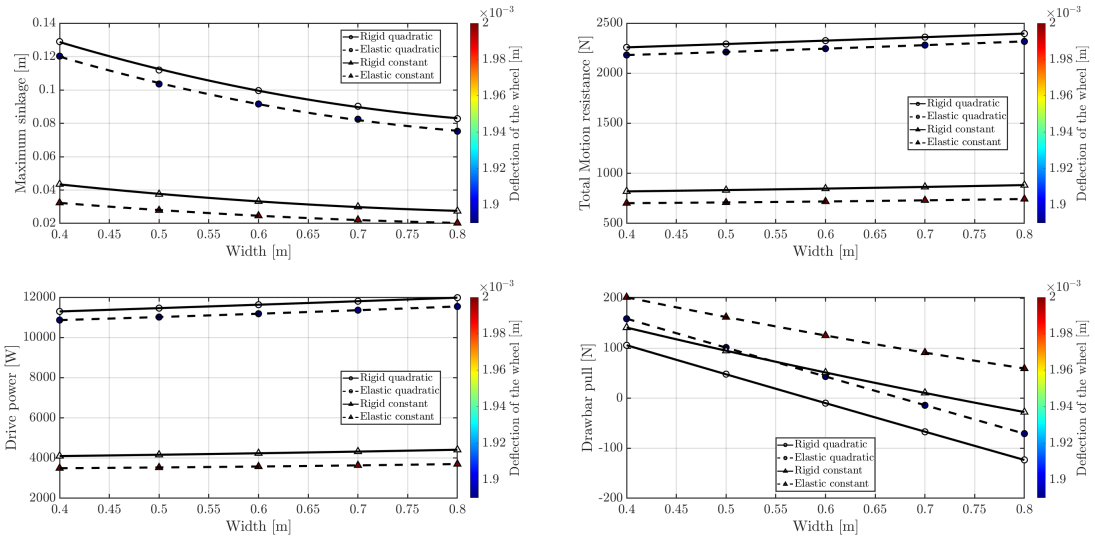

Figure 4.3: Comparison of two approximate models (quadratic and constant stress distributions) for rigid and elastic wheels. Top left: sinkage versus width; top right: resistance versus width; bottom left: drive power versus width; bottom right: drawbar pull versus width. The color bar highlights the effect of wheel deflection.

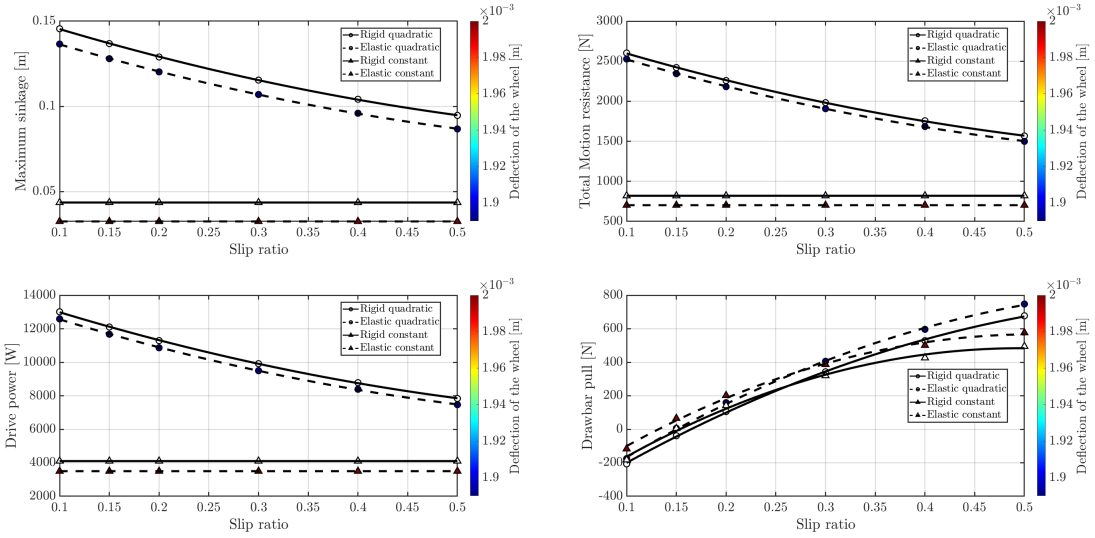

Figure 4.4: Comparison of two approximate models (quadratic and constant stress distributions) for rigid and elastic wheels. Top left: sinkage versus slip; top right: resistance versus slip; bottom left: drive power versus slip; bottom right: drawbar pull versus slip. The color bar highlights the effect of wheel deflection.

Fig. 4.4 show how the slip ratio affects traction performance and power demand for the four modelling cases. As expected, drawbar pull increases with slip ratio and then tends to saturate at higher slip values. This means that, beyond a certain point, increasing slip produces only a limited gain in traction while more energy is dissipated in the soil. At low slip, some configurations show negative drawbar pull, meaning that the available traction is not enough to overcome the total motion resistance. Once a threshold slip value is reached, the drawbar pull becomes positive and then continues to increase.

For the quadratic model, drive power shows the opposite trend and decreases as slip increases. This is consistent with the reduction in effective rolling resistance as the wheel contact changes from mainly rolling to a more shear-dominated condition. By contrast, the uniform approximation shows a non existent dependence on slip, which reflects the formulas used in the simplified stress model.

Total motion resistance decreases monotonically with slip ratio in both models, and the compliant wheel always shows lower resistance than the rigid wheel. Maximum sinkage remains constant over the analysed slip range, suggesting that sinkage is mainly controlled by vertical load balance and contact geometry rather than by the longitudinal shear state. Overall, the results show a clear trade-off between traction and slip: increasing slip improves drawbar pull, but this benefit gradually saturates. Therefore, the most effective operating condition is close to the minimum slip level that still ensures positive drawbar pull, while avoiding unnecessary energy losses and excessive soil disturbance.

Fig. 4.5 shows the sensitivity of the traction performance to vehicle mass (and therefore to the nominal wheel load). As the vehicle weight increases, maximum sinkage rises markedly for all cases, reflecting the nonlinear load–sinkage behaviour predicted by Bekker-type relations. The associated increase in terrain deformation produces a proportional growth in total motion resistance, driven primarily by compaction and bulldozing contributions.
As a direct consequence, the required drive power increases approximately linearly with vehicle weight at fixed speed, consistent with $P \approx R_{\text{all}}\, v$ when resistive terms dominate.
Wheel compliance provides a systematic, though moderate, benefit by enlarging the effective contact area and reducing pressure peaks, thereby lowering sinkage and resistance compared to the rigid wheel at the same load.
Drawbar pull also increases with vehicle weight, indicating that the traction capacity grows with normal load; however, the presence of negative drawbar pull at low masses highlights operating points where available traction is insufficient to overcome resistive losses under the selected conditions.

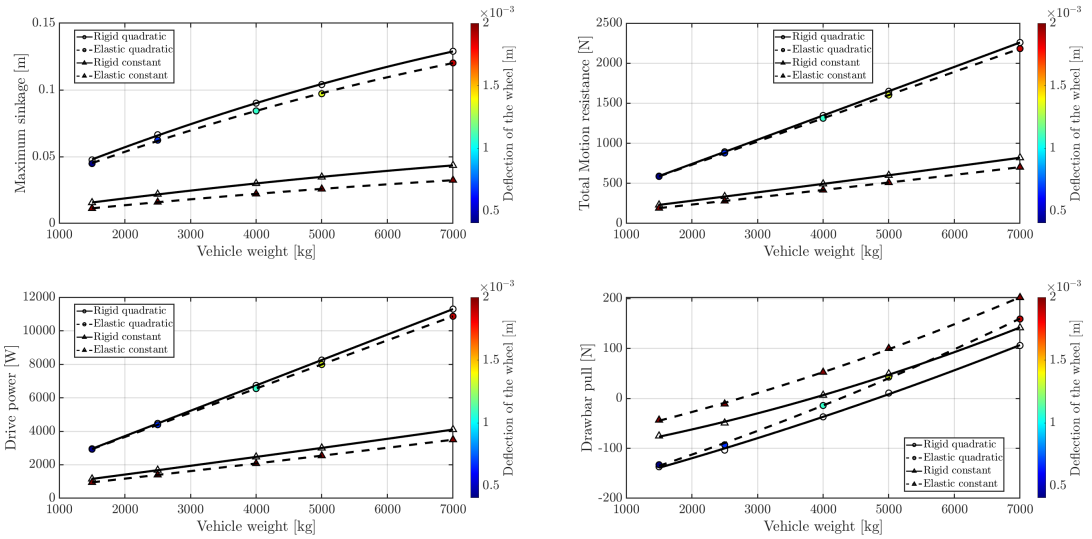

Figure 4.5: Comparison of two approximate models (quadratic and constant stress distributions) for rigid and elastic wheels. Top left: sinkage versus vehicle weight; top right: resistance versus vehicle weight; bottom left: drive power versus vehicle weight; bottom right: drawbar pull versus vehicle weight. The color bar highlights the effect of wheel deflection.

The colour scale provides a direct indication of the wheel deflection δ associated with each operating point. Noticeable variations in the colour map occur only when load-related parameters are swept (i.e., *vehicle weight* and *number of wheels*); in these cases, the quadratic model highlights the expected linear dependence of deflection on the nominal wheel load. For the compliant wheel, δ increases monotonically with vehicle mass, as predicted by the adopted linear stiffness relation $\delta = W/K_t$: a higher rover weight increases the load carried by each wheel and therefore leads to a larger structural deformation, with higher resistances but also better traction performances.

Fig. 4.6 highlight the impact of the number of wheels (i.e., wheel load sharing) on mobility performance. Increasing N_w reduces the nominal load per wheel and therefore decreases maximum sinkage, in agreement with Bekker-type load–sinkage scaling. The reduced terrain deformation also lowers the total motion resistance, primarily through a reduction of compaction and bulldozing losses. As a consequence, the required drive power decreases with N_w at fixed speed.

The drawbar pull, however, degrades as N_w increases: although resistance is reduced, the traction capacity per wheel decreases with the lower normal load and smaller shear interface displacements, leading to a reduced traction margin. This

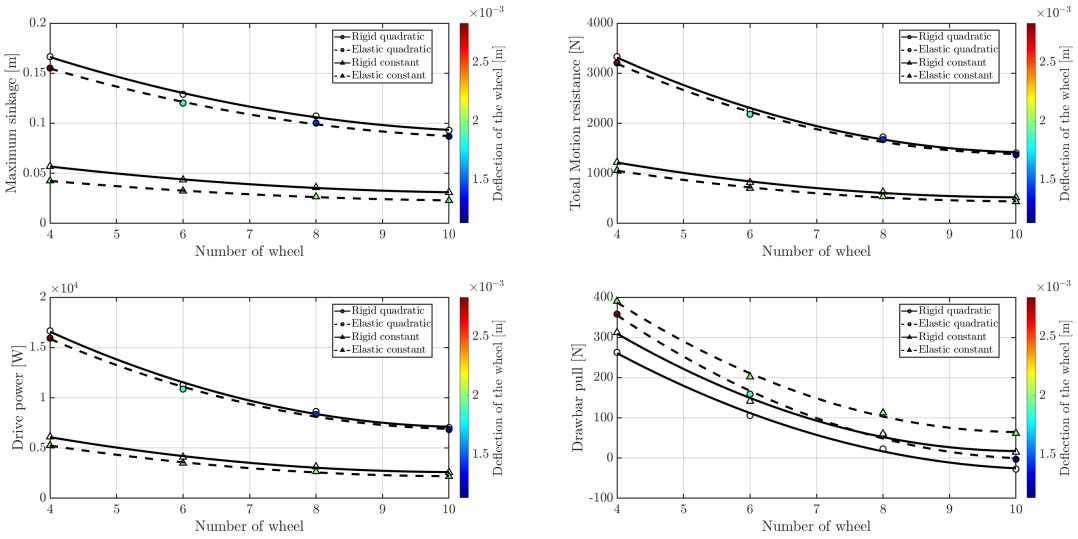

Figure 4.6: Comparison of two approximate models (quadratic and constant stress distributions) for rigid and elastic wheels. Top left: sinkage versus number of wheel; top right: resistance versus number of wheel; bottom left: drive power versus number of wheel; bottom right: drawbar pull versus number of wheel. The color bar highlights the effect of wheel deflection.

effect is evident in the high-N_w cases, where the drawbar pull approaches zero or becomes slightly negative for the higher-fidelity model, indicating operating points close to the traction limit. Wheel compliance provides a consistent benefit across N_w by increasing the effective contact area and reducing stress peaks, improving drawbar pull while simultaneously reducing sinkage and resistance. As observed in the previous sensitivities, the uniform approximation reproduces the qualitative trends but remains systematically more optimistic than the quadratic stress model.

Fig. 4.7 confirms the expected kinematic scaling of energetic demand: for a given configuration, drive power increases approximately linearly with forward velocity, consistent with $P = T\,\omega \approx R_{\text{all}}\,v$ when the resistive force is weakly dependent on speed. The compliant-wheel cases maintain a lower power requirement due to the reduced motion resistance, while the simplified formulation yields the lowest predicted power levels. Only the power map is reported, since velocity directly affects this metric alone. This is a consequence of treating velocity and slip ratio as independent design variables, i.e., decoupling the longitudinal velocity from the slip condition.

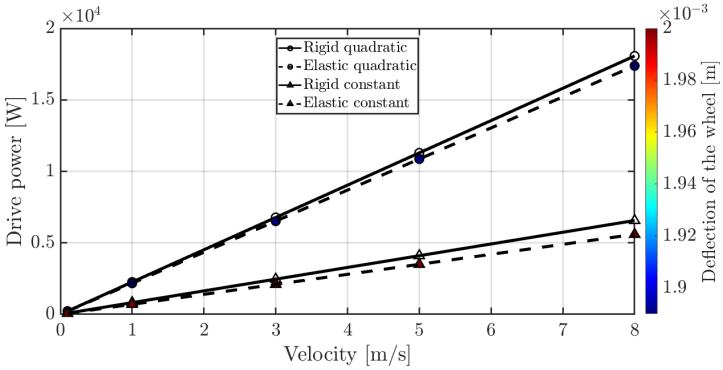

Figure 4.7: Comparison of two approximate models (quadratic and constant stress distributions) for rigid and elastic wheels. Drive power versus motion velocity.

Two-variable sensitivity analysis

The same sensitivity analysis is also carried out by varying two design parameters, to assess how their combined effect can influence performance compared with varying each parameter individually. The fixed values used are the same as in the single-variable case.

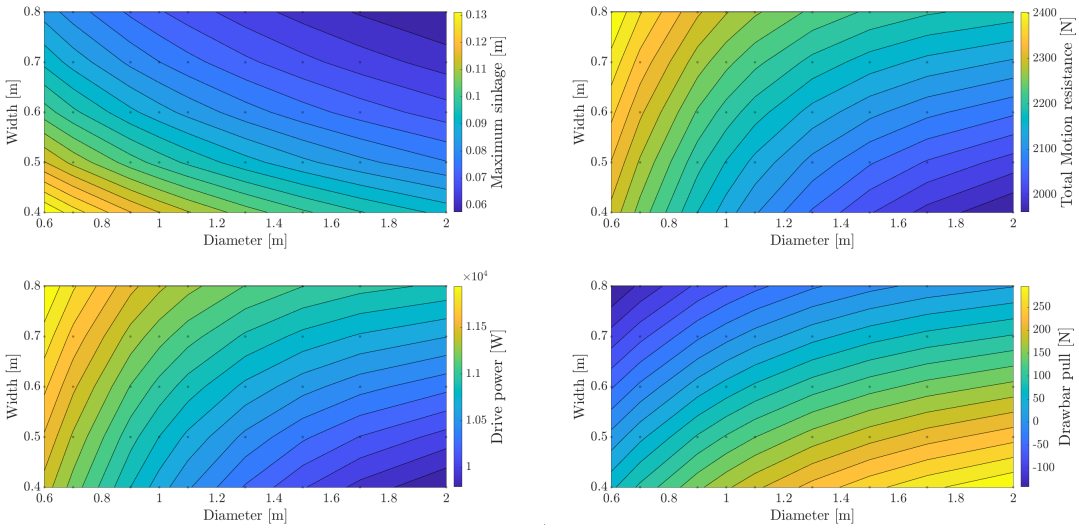

Figure 4.8: Contour plot based on the flexible wheel quadratic approximation model. Top left: sinkage versus diameter and width; top right: resistance versus diameter and width; bottom left: drive power versus diameter and width; bottom right: drawbar pull versus diameter and width.

The contour maps 4.8 provide a compact trade-space representation of the flexible-wheel quadratic model. Increasing diameter consistently reduces maximum sinkage, total motion resistance and drive power, confirming that d is the primary level for improving mobility and energetic efficiency on soft regolith. The sinkage reduction is most pronounced at small diameters, while gains become progressively smaller at larger d.
Wheel width mainly acts on sinkage control: larger b decreases sinkage through lower average ground pressure. However, the drawbar-pull map highlights how the traction improves strongly with diameter but tends to decrease with increasing width in the explored range. Overall, the maps indicate an optimal design region at high d and moderate b, where resistance and power are minimized while maintaining a favourable drawbar-pull margin.

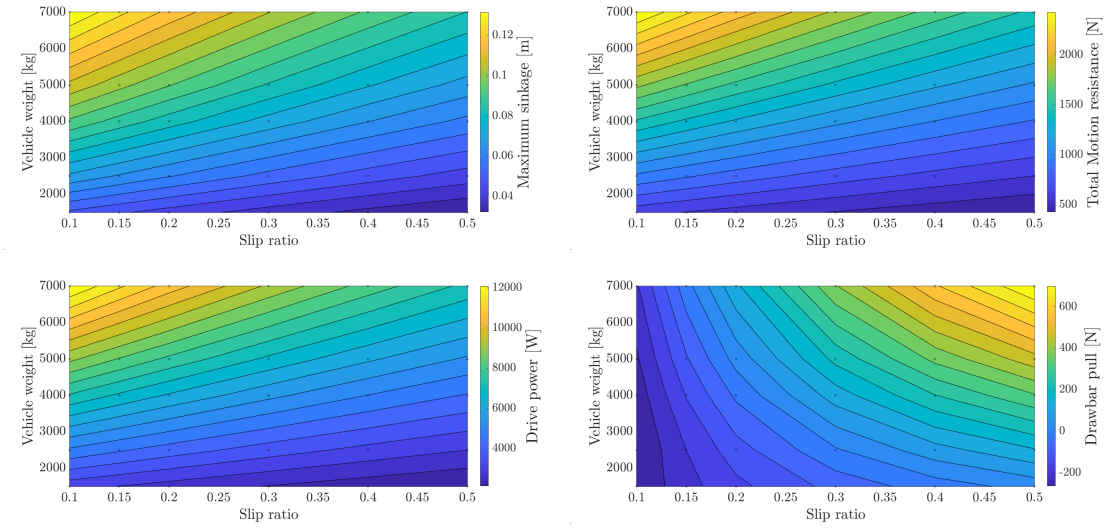

Figure 4.9: Contour plot based on the flexible wheel quadratic approximation model. Top left: sinkage versus slip and rover mass; top right: resistance versus slip and rover mass; bottom left: drive power versus slip and rover mass; bottom right: drawbar pull versus slip and rover mass.

The contour maps 4.9 highlight the coupling of normal load and shear mobilisation on soft regolith. As expected, increasing vehicle weight increases maximum sinkage, total motion resistance and drive power across the entire slip range, reflecting the nonlinear load–sinkage response and the associated growth of compaction and bulldozing losses. In contrast, sinkage is only weakly affected by slip ratio, indicating that the vertical equilibrium (and thus h_f) is primarily governed by the nominal wheel load rather than by the longitudinal shear state in the considered model.

Drawbar pull shows the clearest coupling between the two parameters. At low slip, the drawbar pull is negative or close to zero for heavier vehicles, meaning that the available traction is insufficient to overcome resistive losses under those operating conditions. As slip increases, drawbar pull improves and becomes positive, consistent with progressive shear stress mobilisation (Janosi–Hanamoto) and the approach to a saturation regime. The maps therefore identify a slip threshold that increases with vehicle weight: heavier rovers require higher slip to generate a positive traction margin, at the cost of reduced efficiency. Overall, the trade-space suggests operating at the minimum slip level that ensures positive drawbar pull for the expected vehicle mass, while prioritising mass management to limit sinkage-driven resistance and power demand.

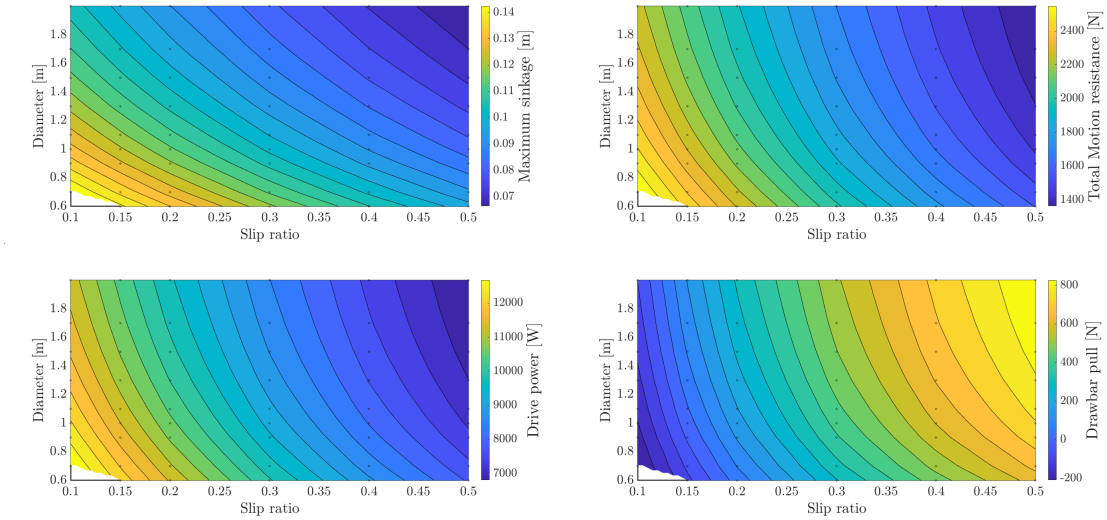

Figure 4.10: Contour plot based on the flexible wheel quadratic approximation model. Top left: sinkage versus slip and diameter; top right: resistance versus slip and diameter; bottom left: drive power versus slip and diameter; bottom right: drawbar pull versus slip and diameter.

The contour maps 4.10 show the combined effect of contact geometry and shear mobilization on soft regolith. The maps indicate that increasing d expands the feasible low-slip operating envelope, enabling positive drawbar pull.

The power map 4.11 highlights how drive power increases approximately linearly with velocity, while increasing the number of wheels reduces the power demand by lowering the nominal load per wheel and, in turn, the associated motion resistance. This map is therefore useful for selecting a drivetrain operating range once a wheel number is fixed by system-level constraints (packaging, redundancy and mobility

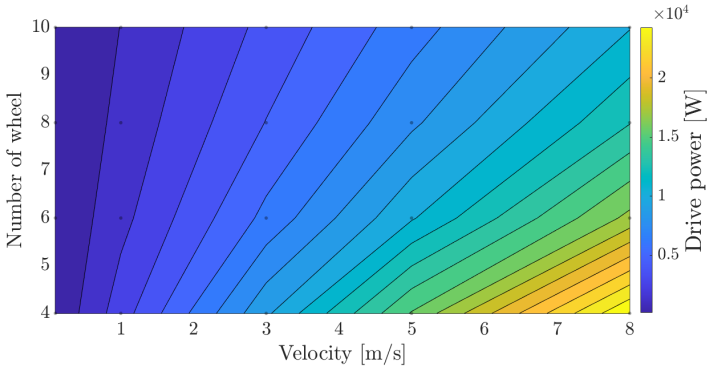

Figure 4.11: Contour plot based on the flexible wheel quadratic approximation model. Drive power versus motion velocity and number of wheels.

requirements).

Finally, Tab. 4.3 summarises the most favourable design space for each variable to be considered when selecting the optimal configuration. In any case, the wheel should be elastic, as this solution consistently outperforms the rigid one on soft terrain.

Table 4.3: Recommended design choices for a pressurised lunar rover traction system on soft regolith, derived from the sensitivity analysis.

Design variable	**Recommended choice**
Wheel diameter d	Large
Wheel width b	Moderate
Number of wheels N_w	Intermediate
Vehicle mass (or wheel load)	As low as permitted by mission constraints
Slip ratio s	Moderate, close to the minimum value ensuring positive drawbar pull
Forward speed v	Selected according to mission and energy constraints

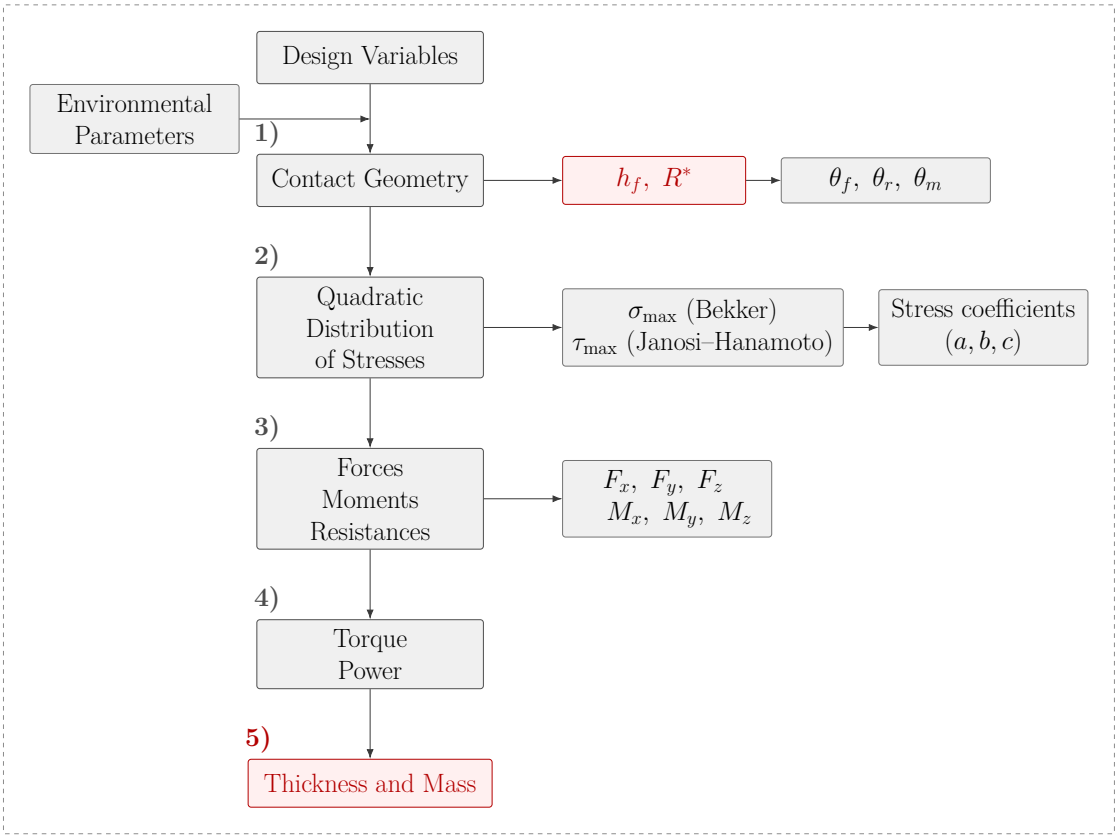

Figure 4.12: Analytical model flowchart

4.3 Analytical parametric study

After the sensitivity analysis, the analytical assessment is extended to a parametric study. The objective is to generate a matrix of feasible configurations by varying a finite range of design variables . This configuration matrix provides the basis for selecting an optimal solution among many candidates through the use of figures of merit. The procedure can be regarded as an initialization step that will subsequently support the higher-fidelity numerical analysis.

The flowchart shown in Figure 4.12 summarizes the logical sequence implemented in the MATLAB code to generate the configuration matrix for the parametric study. First, all design variables are defined (Table 4.1) and the environmental parameters (lunar regolith) are specified. An iterative loop is then executed to sweep the configuration parameters one-by-one, compute the required outputs for each candidate configuration, and store the corresponding results in the matrix.
In the flowchart, the elements highlighted in red indicate the additional steps

Table 4.4: Material properties adopted for wheel sizing (Aluminium 7075).

Property	**Symbol**	**Value**
Young's modulus	E	7.24×10^{10} Pa
Poisson's ratio	ν	0.30
Density	ρ	2700 kg m^{-3}

introduced to account for wheel deflection, i.e., the transition from a rigid-wheel formulation to a deformable-wheel formulation.

Within the loop, the wheel–terrain contact geometry is evaluated, as detailed in Figures 4.13 and 4.15. In particular, the maximum sinkage h_f, the entry angle θ_f, the exit angle θ_r and the angle associated with the maximum normal stress θ_m are computed. The stress distribution is then characterised: the peak values are estimated using the semi-empirical formulations by Bekker (normal pressure) and Janosi–Hanamoto (shear stress). These maxima are subsequently used to determine the stress coefficients to be employed in the analytical integrations for forces and moments. All resistance contributions are evaluated in order to estimate the drive torque and the corresponding power required to sustain forward motion.

The final step is the assessment of the wheel thickness and mass, which enables the definition of an additional structural figure of merit. From a computational and modelling standpoint, this step is meaningful only for the flexible-wheel case, as the adopted sizing relations explicitly depend on the wheel deflection.
Specifically, the wheel thickness is computed using the quasi-static deformation formula for a thin-walled ring, considered equivalent to the simplified wheel geometry under compressive loading, as reported in [20].
Material properties must therefore be specified, since they directly enter the sizing formulation. The material selection is guided by the influence of radiation exposure, pressure conditions and temperature extremes on structural integrity in an extra-terrestrial environment. Metallic alloys are selected (Aluminium 7075; Table 4.4), which are typically preferred over polymeric solutions for lunar mobility applications [17, 19].

Finally, the wheel mass is estimated based on geometrical and physical considerations consistent with the adopted wheel cross-section model.

$$thickness = \sqrt[3]{\frac{1.776\, W_w\, r^3}{E\, b\, \delta}} \tag{4.1}$$

$$mass = \rho\, \pi \left(r^2 - (r - t)^2 \right) b \tag{4.2}$$

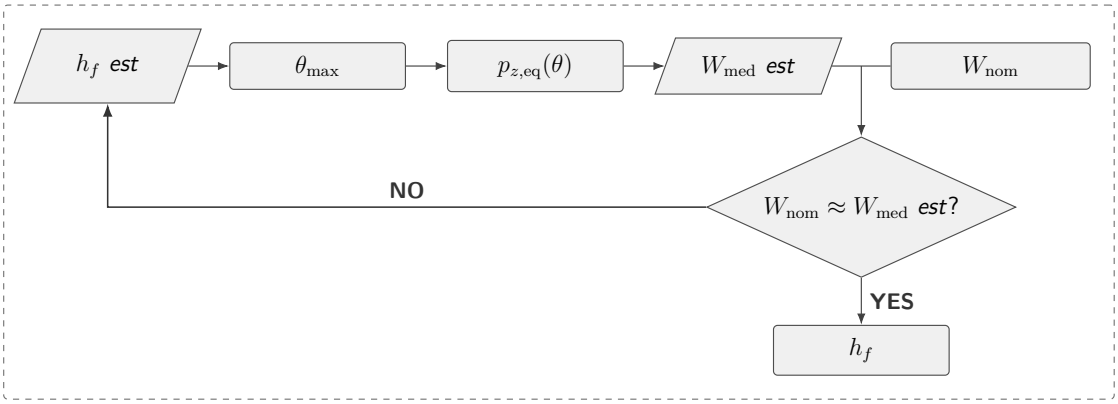

Figure 4.13: Flowchart of the iterative process for determining the maximum sinkage h_f from vertical equilibrium (rigid wheel).

4.3.1 Contact geometry

The evaluation of the wheel–terrain contact geometry represents the most delicate step of the overall analytical procedure and must be treated differently for rigid and deformable wheels.

Figure 4.13 illustrates the iterative scheme adopted to compute the maximum sinkage h_f for a rigid wheel. The method is based on vertical equilibrium and follows an approach similar to that proposed in [18], where it is used for the contact angle estimation.

A trial range for the maximum sinkage is prescribed, spanning from zero up to the wheel radius, i.e., $h_f\mathrm{est} \in (0, r]$. For each candidate value of $h_f\mathrm{est}$, an average sinkage is first evaluated and the corresponding contact angles θ_f (entry), θ_r (exit), and θ_m (angle associated with the maximum normal stress) are determined. The maximum normal pressure is then computed using the Bekker formulation, and an equivalent vertical pressure distribution $p_{z,\mathrm{eq}}$ is defined accordingly. Finally, by integrating over the contact patch, an estimation of the vertical wheel load $W_{\mathrm{med}}\mathrm{est}$ is obtained.

The normal pressure σ is the dominant contribution to the vertical pressure distribution p_z along the z-axis; therefore, the equivalent pressure $p_{z,\mathrm{eq}}$ can be described in terms of σ alone. Moreover, for soils characterised by relatively large sinkage exponents ($n \geq 1$), the actual vertical pressure profile, which reaches its maximum at θ_m and vanishes at θ_f and θ_r, can be accurately approximated by a linear function. Consequently, an entry-angle estimator based on a linear approximation of p_z provides an effective and computationally efficient solution

(Figure 4.14).

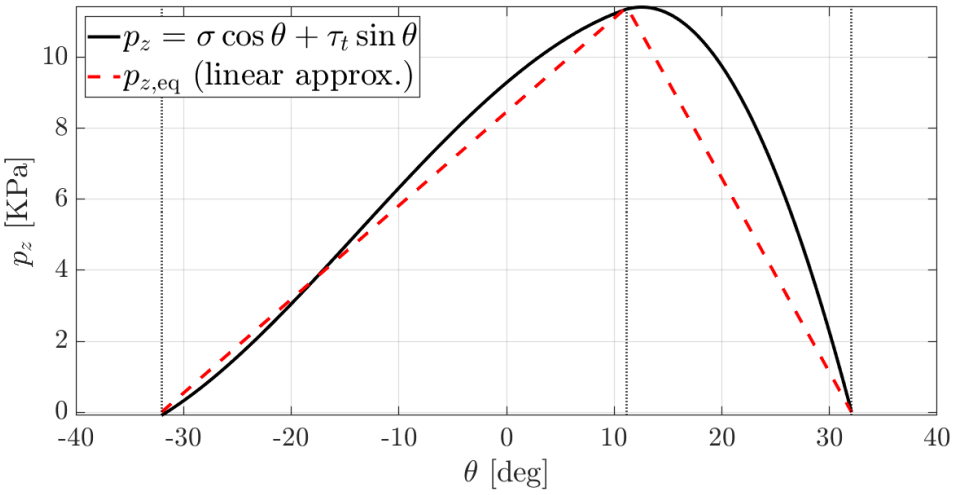

Figure 4.14: Comparison of the normal pressure distributions along the contact patch: (*original*) versus equivalent linear approximations.

$$p_z(\theta) = \sigma cos(\theta) + \tau_t sin(\theta) \tag{4.3}$$

$$p_{z,eq}(\theta) = \sigma\theta_{eq}(\theta) \tag{4.4}$$

Here, $\theta_{\text{eq}}(\theta)$ is the equivalent angle of θ.

$$\theta_{\text{eq}}(\theta) = \begin{cases} \dfrac{\pi}{2}\dfrac{\theta - \theta_r}{\theta_m - \theta_r}, & \theta_r \leq \theta \leq \theta_m, \\ \pi - \dfrac{\pi}{2}\dfrac{\theta_f - \theta}{\theta_f - \theta_m}, & \theta_m \leq \theta \leq \theta_f. \end{cases} \tag{4.5}$$

The vertical load estimation W_{med}est is, then, obtained by integrating the equivalent pressure distribution over the contact patch, i.e., along the contact angle and scaled by the wheel radius and wheel width. The maximum sinkage h_f is finally determined through the bisection method: the trial value of h_f is iteratively updated until the estimated vertical load matches the nominal wheel load, within a prescribed tolerance.

Figure 4.15 illustrates the iterative process adopted to compute the maximum sinkage h_f for an elastic wheel, based on balancing the soil vertical reaction force and the tyre vertical force. A representative value of the vertical tyre stiffness is imposed ($K_t = 10^6$), from which the wheel deflection is computed as a function of the nominal wheel load. The corresponding tyre vertical force is estimated.

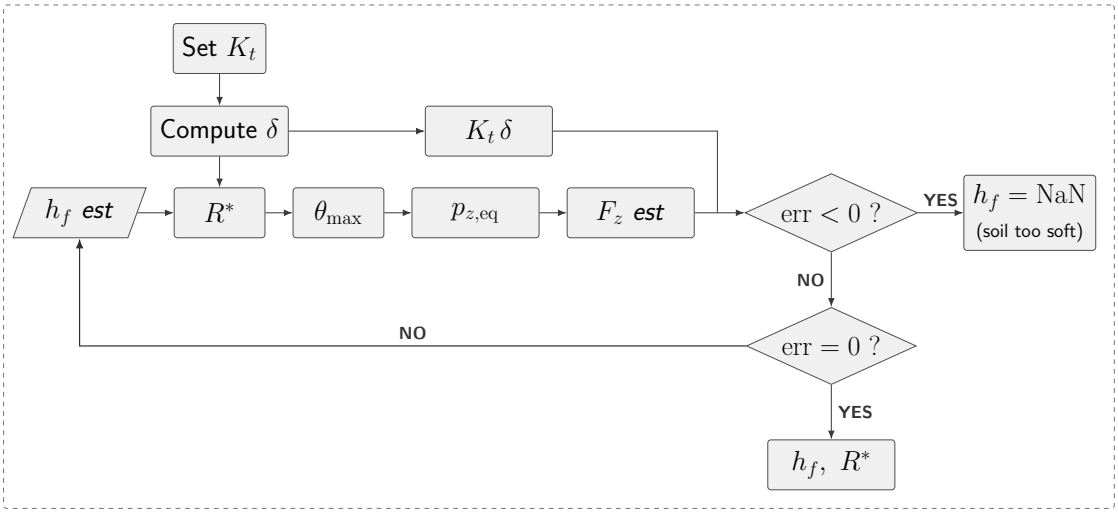

Figure 4.15: Flowchart of the flexible-wheel substitute-circle equilibrium logic.

By means of the substitution-circle method, the effective radius R^* associated with the substitute circle is then evaluated, as discussed in Subsection 3.3.3. The procedure adopted to estimate the soil vertical reaction force $F_{z,\mathrm{est}}$ follows the same logic used for the rigid-wheel case; however, in the elastic-wheel formulation all geometric quantities and the subsequent force evaluation are performed using the updated radius R^*.

$$F_{z,est} = br \int_{\theta_r^*}^{\theta_f^*} \sigma(\theta^*) \cos\theta^* \, \mathrm{d}\theta^* \tag{4.6}$$

$$F_{z,t} = K_t \, \delta \tag{4.7}$$

$$\frac{r^*}{r} = \left(\sqrt{1 + \frac{\delta}{h_f}} + \sqrt{\frac{\delta}{h_f}} \right)^2 \tag{4.8}$$

These three equations are solved iteratively until the residual is sufficiently small. The residual is defined as

$$\mathrm{error} = F_{z,\mathrm{est}} - F_{z,t}. \tag{4.9}$$

Convergence is achieved when the |error| falls below a prescribed tolerance.
If error < 0, the terrain is excessively compliant for the considered wheel configuration: even at the maximum admissible sinkage the soil vertical reaction remains lower than the vertical tyre force, i.e., $F_{z,\mathrm{est}} < F_{z,t}$. In this condition the configuration is deemed infeasible (the soil cannot sustain the load and stable forward motion cannot happen).

4.3.2 FoM

The figures of merit are included directly in the configuration matrix, since they provide a convenient quantitative indicator of system quality and therefore enable an objective comparison and selection of the optimal configuration. In particular, three figures of merit were defined in order to select the best configurations among those evaluated: *maximum drawbar pull*, *minimum power consumption*, and *minimum wheel mass*. To enable a consistent comparison across the design space, each quantity is normalized to the interval [0,1] using a min–max scaling. Drawbar pull is treated as a benefit metric and therefore scaled such that larger values correspond to higher scores. Conversely, drive power and wheel mass are treated as cost metrics and are normalized using an inverted min–max scaling, so that lower values yield higher scores.
Therefore, an overall Figure of Merit (FoM) is defined as an equally weighted combination of the three normalized terms:

$$\mathrm{FoM} = \frac{1}{3}\,\mathrm{DP}_{\mathrm{norm}} + \frac{1}{3}\,\mathrm{P}_{\mathrm{norm}} + \frac{1}{3}\,\mathrm{M}_{\mathrm{norm}}. \tag{4.10}$$

Finally, the configuration table is sorted in descending order of FoM, so that the highest-ranked entries identify the configurations providing the best trade-off between traction capability, power demand and wheel mass.

4.3.3 Result analytic analysis

The following assumptions should always be kept in mind when interpreting the results: a cylindrical wheel geometry is considered; the terrain slope angle is assumed to be zero (although this parameter can also be varied within the model) and the exit angle is taken equal to the entry angle. The latter assumption can likewise be relaxed if a specific mission path is considered, allowing the two angles to be treated independently.

In addition, a set of design requirements is imposed in order to make the locomotion system as representative as possible of a realistic pressurized lunar rover configuration.

1. The wheel shall be elastic because if there is deflection, the contact area increases, the ground pressure decreases and the wheel performance improve.

2. The nominal slip ratio is fixed at $s = 0.2$ because, according to [21], this value is generally recommended for lunar rovers. In particular, the literature reports that for the Lunar Roving Vehicle a recommendation of $s \leq 0.2$ is usually adopted. Lower average slip values are observed for the Soviet Lunokhod over

nominal traverses, whereas significantly higher values may occur in extreme conditions, such as crater escape ($s \geq 0.4$) or emergency situation ($s > 0.5$).

3. The rover mass is fixed at 7000 kg, corresponding to the upper limit of the investigated range. This choice is made in order to assess wheel performance under the most demanding loading condition considered in the study and to ensure that the final design remains feasible even in the most critical case.

4. The forward velocity is fixed at 3 m/s in order to evaluate the locomotion system under a realistic traverse condition for a pressurized lunar rover.

The analysis of the final design matrix is carried out by filtering the configurations according to a set of different criteria. First, all cases with non-positive drawbar pull ($DP \leq 0$) are discarded, together with configurations characterized by excessively heavy wheels ($m_w > 100$ kg). The remaining solutions are, then, compared on the basis of the following performance indicators: minimum sinkage, maximum drawbar pull and available traction, minimum total motion resistance (with particular emphasis on the bulldozing resistance, which represents the dominant resistance component for wheels of such large dimensions), minimum drive torque, minimum drive power and minimum wheel mass. Finally, the metric defined in the previous section is also taken into account in order to support the identification of the most balanced overall solution.

Table 4.5 summarises the final trade-off among the four most promising wheel configurations. The comparison highlights the competing effects of wheel diameter, wheel width and number of wheels on mobility performance, energetic demand and structural mass.
Configuration 1 provides the best global compromise among the analysed cases and therefore is selected as the final design solution. Although its drawbar pull is lower than the other, it remains positive and therefore ensures feasible traction conditions. At the same time, it exhibits the lowest total motion resistance, the lowest drive power requirement and the highest figure of merit. The corresponding sinkage is also acceptable and it remains consistent with a viable operating condition on soft

	d **[m]**	b **[m]**	N_w	h_f **[m]**	DP **[N]**	R_{tot} **[N]**	T_d **[Nm]**	P_d **[W]**	m_w **[kg]**	**FoM**
1	1.0	0.4	8	0.0970	73	1651	823	4939	66	0.6123
2	1.0	0.4	6	0.1165	182	2148	1070	6421	66	0.5946
3	0.9	0.4	6	0.1202	159	2182	978	6519	53	0.5879
4	0.9	0.5	6	0.1036	102	2212	991	6609	62	0.5459

Table 4.5: Comparison of the four most relevant wheel configurations considered in the final trade-off analysis.

regolith.

The following consideration can be made about the remaining configurations.

By distributing the vehicle load over a larger number of wheels, the contact load acting on each wheel is reduced, leading to lower sinkage and lower motion resistance. However, configurations providing a larger tractive margin may still exhibit a less balanced overall performance because of the associated increase in drive torque and power demand.

A smaller wheel diameter leads to increased sinkage and higher resistance. Although the corresponding wheel mass is reduced, this advantage is not sufficient to compensate for the deterioration in energetic performance and overall efficiency.

Similarly, increasing wheel width does not provide a sufficiently favourable improvement in the overall design trade-off. Within the analysed range, the benefits associated with the reduction in sinkage are offset by penalties in resistance, power demand and mass.

Overall, the outcomes of this trade-off analysis are fully consistent with the trends already identified in the previous sensitivity analysis.

The geometric characteristics and performance metrics of this specific configuration are presented in detail in Tab.4.6, 4.7 ed in Fig.4.16, 4.17, 4.18.

Parameter	**Value**
Wheel diameter d [m]	1.0
Wheel width b [m]	0.4
Number of wheels N_w [-]	8
Slip ratio s [-]	0.2
Forward velocity v [m/s]	3
Vehicle mass m_v [kg]	7000
Weight on each wheel [N]	1417.5
Wheel thickness [m]	0.0197
Wheel mass m_w [kg]	65.58
Wheel deflection [m]	0.00142

Table 4.6: Main design parameters of the selected wheel configuration (1).

The results shown emphasize the non-uniform nature of the wheel–soil contact stresses. The normal stress distribution governs the main load transfer, while the tangential components are concentrated in the effective contact region where traction and shear are developed. The stress distributions are coherent with the quadratic theory used for the stress computation.

Parameter	Value
Maximum traction [N]	1724.06
Drawbar pull DP [N]	72.96
Entry contact angle [deg]	-32.05
Exit contact angle [deg]	32.05
Maximum stress angle [deg]	11.19
Maximum sinkage h_f [m]	0.0970
Contact patch area [m^2]	0.2702
Maximum normal stress [Pa]	9954.99
Maximum longitudinal shear stress [Pa]	8235.89
Maximum lateral shear stress [Pa]	5096.65
Soil compaction resistance [N]	308.93
Bulldozing resistance [N]	1306.73
Rolling resistance [N]	35.44
Total motion resistance R_{tot} [N]	1651.10
Drive torque T_d [Nm]	823.21
Drive power P_d [W]	4939.26
Average pressure [Pa]	5246.82

Table 4.7: Contact and performance metrics of the selected wheel configuration (1).

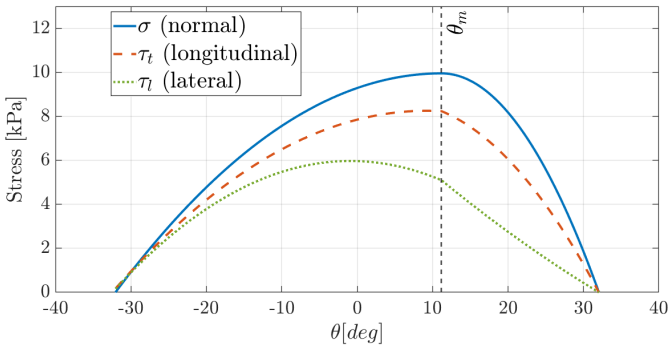

Figure 4.16: Stress distribution along the contact patch

Hub sizing

In order to size the hub of the wheel, a previous actuator electromechanical sizing is carried out starting from the requirements associated with the selected configuration. (Results summarized in Tab. 4.8)
According to the terramechanics analysis, the nominal wheel-side requirements are a drive torque of 823 Nm and a drive power of 4.94 kW. Since the wheel diameter is $d = 1.0$ m and the forward speed is $v = 3\ \mathrm{m\,s^{-1}}$, the wheel rotational speed is

$$n_w = \frac{60\,v}{\pi d} = \frac{60 \cdot 3}{\pi \cdot 1} \approx 57.3 \text{ rpm}. \tag{4.11}$$

A design margin of approximately 20% was then introduced in order to account

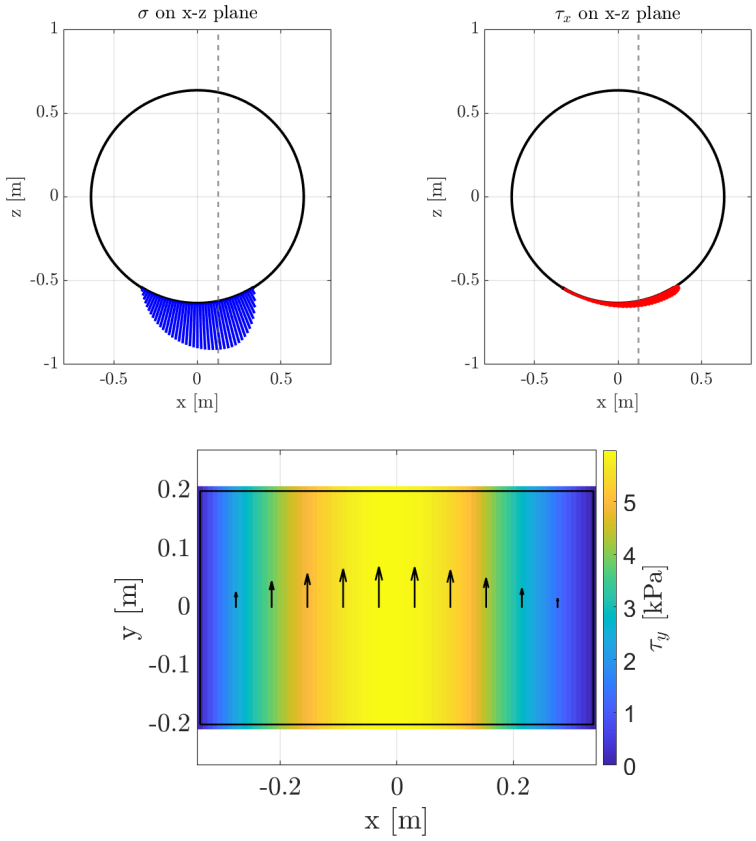

Figure 4.17: Stress distribution along the wheel (2D). Top left: σ on x-z plane; top right: τ_x on x-z plane; bottom: τ_y on x-y plane (top view)

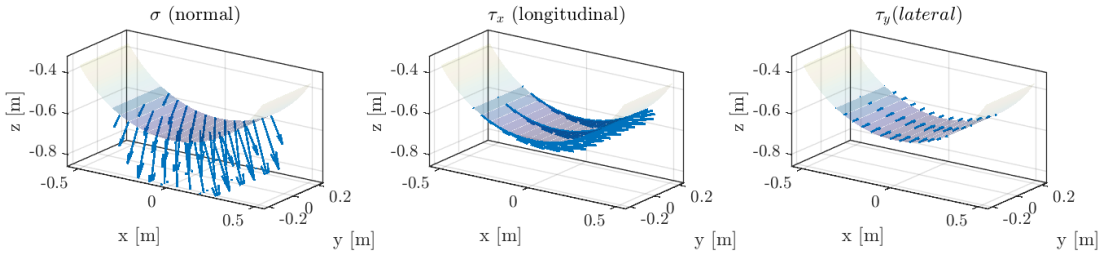

Figure 4.18: Stress distribution along the wheel (3D)

for modelling uncertainty and off-nominal terrain conditions. This leads to the

Parameter	**Value / selection**
Selected wheel configuration	$d = 1.0$ m, $b = 0.4$ m, $N_w = 8$
Nominal wheel torque requirement	$T_d = 823$ Nm
Nominal wheel power requirement	$P_d = 4.94$ kW
Wheel rotational speed at $v = 3\ \mathrm{m\,s^{-1}}$	$n_w \approx 57.3$ rpm
Design torque with margin	$T_{d,\mathrm{des}} \approx 990$ Nm
Design power with margin	$P_{d,\mathrm{des}} \approx 5.9$ kW
Actuator architecture	Brushless servo motor + high-ratio reduction in the hub
Motor family	Kollmorgen AKM2G servo motor
Reducer family	Harmonic Drive CSG-GH
Selected reduction ratio	$i = 80{:}1$
Required motor speed	$n_m \approx 4580$ rpm
Required motor torque	$T_m \approx 14.6$ Nm
Minimum internal hub diameter	≥ 220 mm

Table 4.8: Sizing of actuator and the wheel hub for the selected configuration.

following design values at wheel level:

$$T_{w,\mathrm{des}} = 1.2\,T_w \approx 1.2 \cdot 823 \approx 990 \text{ Nm} \tag{4.12}$$

$$P_{w,\mathrm{des}} = 1.2\,P_w \approx 1.2 \cdot 4.94 \approx 5.9 \text{ kW} \tag{4.13}$$

The required wheel torque is too high for a compact direct-drive architecture hub motor. A more realistic option is therefore a geared in-wheel actuator, consisting of a brushless servo motor coupled with a high-ratio reducer integrated inside the wheel hub.
Assuming a transmission ratio equal to

$$i = 80{:}1,$$

the corresponding motor speed becomes

$$n_m = i\,n_w \approx 80 \cdot 57.3 \approx 4580 \text{ rpm}, \tag{4.14}$$

which is compatible with the operating range of industrial servo motors such as the Kollmorgen AKM2G family [22].
Assuming an overall reducer efficiency of

$$\eta \approx 0.85,$$

the motor torque required to deliver the design wheel torque is

$$T_m = \frac{T_{w,\mathrm{des}}}{i\,\eta} = \frac{990}{80 \cdot 0.85} \approx 14.6 \text{ Nm}. \tag{4.15}$$

For this reason, a motor class capable of providing at least about 13–16 Nm continuously is a suitable target for the selected configuration.

For the reducer, the Harmonic Drive CSG-GH family is appropriate because it is available in ratios from 50:1 to 160:1 and it is compatible with servo motors up to the kilowatt range. The size 65 gearhead is characterized by an outside dimension of roughly 220–230 mm [23]. This gearbox envelope sets the lower bound for the internal wheel-hub size. A realistic engineering target is in the range of 240–260 mm in order to accommodate bearings, housing thickness, seals, thermal paths and assembly clearances.

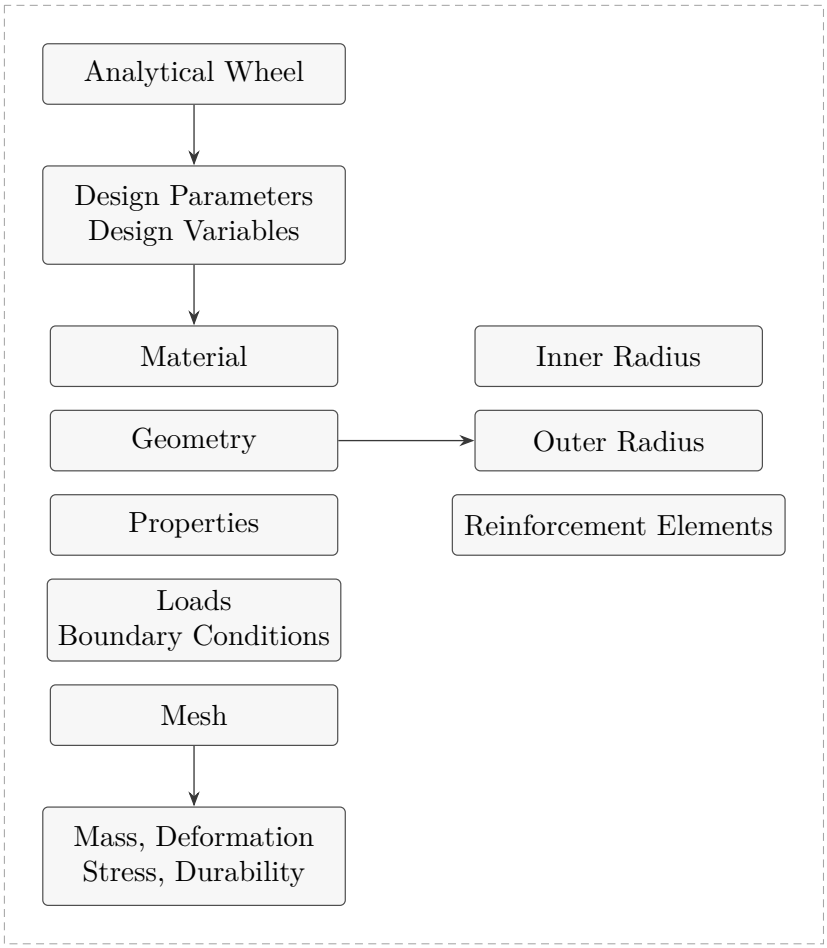

Figure 4.19: Numerical model flowchart

4.4 FEM parametric study

Following the analytical selection of the wheel based on mobility performance, the study proceeded with the numerical and manufacturing-oriented selection of the wheel architecture.

A common parametric workflow (Fig. 4.19) is adopted for the generation and structural analysis of the wheel architectures considered in this work. By initializing the numerical procedure with the parameters obtained from the preliminary analytical–terramechanics assessment, it is possible to investigate the structural response of each configuration under consistent operating conditions.

For each configuration, the main geometric and mechanical input parameters are assigned in MATLAB. These parameters include the outer radius, inner radius, wheel width, thickness of the external ring, thickness of the internal ring, thickness of the reinforcing elements, number of internal reinforcements, vehicle mass, number of wheels and mesh size. On the basis of these inputs, MATLAB automatically generates the Patran session file required to build the corresponding finite element model. The modeling procedure includes the creation of the outer ring, the inner hub, and the internal reinforcing structure, followed by the assignment of material properties and shell properties, the application of loads and boundary conditions and the generation of the surface mesh.

The applied vertical load derives from the total vehicle weight divided by the number of wheels, so that each wheel is analyzed under the corresponding share of the global load. In order to reproduce a more realistic load transfer from the vehicle to the wheel, the load is not applied directly to a single structural node. Instead, a reference point is created at the wheel center and connected to the nodes of the internal hub by means of an MPC/RBE3 constraint. In this way, the imposed vertical force is redistributed over the inner structure, thus avoiding artificial stress concentrations due to a purely nodal load application (Figure 4.20).

Concerning the material modeling, the numerical framework is intentionally defined in a flexible way. The code allows the material assigned to the external ring, the internal ring and the reinforcing elements to be modified independently. Therefore, any material can be associated with each structural part, making the procedure suitable not only for uniform metallic wheels, but also for multi-material configurations. In the present study, the material properties are defined in terms of Young's modulus, Poisson's ratio, density and yield stress, and can be readily updated depending on the selected design scenario.

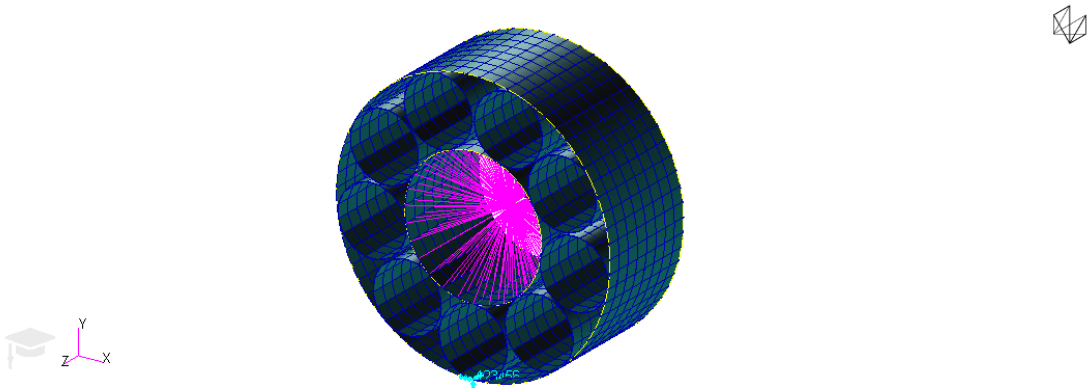

Figure 4.20: Hoop wheel load and constraints

Once the model is generated, the static finite element analysis is executed automatically through MSC Nastran. The main structural outputs are then extracted directly from the output HDF5 file. In particular, the vertical deflection is obtained from the maximum nodal displacement in the loading direction, the wheel stiffness is computed as the ratio between the applied load and the corresponding vertical deflection, the maximum stress is derived from the stress state of the shell elements, the wheel mass is read directly from the model results and the durability index is evaluated as a function of the ratio between the maximum stress and the material yield stress.

Overall, this automated workflow makes it possible to compare the wheel architectures in a systematic and reproducible manner. Starting from the parameters derived from the analytical–terramechanics study, the numerical model provides a coherent framework to assess the structural behavior of each configuration and to support the identification of the most promising solution in terms of strength, stiffness, mass and durability.

4.4.1 Wheel architectures

The selection of the wheel architectures to be investigated is based on both the lunar-rover literature and their compatibility with the lunar environment and mission requirements. Pneumatic wheels are not suitable for lunar applications because rubber materials undergo degradation under prolonged exposure to solar radiation. Rigid wheels, on the other hand, provide poor ride comfort and, as already demonstrated in the previous analyses, generally exhibit worse performance than elastic solutions. Wire-mesh wheels are not easily scalable to heavier vehicles and long-range missions. Similarly, the elliptical wheel and hubless concepts present

significant drawbacks in terms of reliability and specific mass.

On this basis, four wheel architectures are finally selected, as shown in Fig. 4.21 for the numerical investigation: the *hoop spring wheel*, the *modified spiral spring wheel*, the *tweel wheel*, and the *twin-carcasses wheel*.
Since all these concepts belong to the family of elastic wheels, they generally consist of a rigid hub, which houses the electric motor, a flexible rim, typically equipped with grousers and a set of flexible spokes connecting the rim to the hub. The four selected architectures mainly differ in the geometry and orientation of the spokes, which result in different structural layouts. For instance, in hoop-type configurations the spoke axis may be either parallel to the motor axis (as in this work) or tangential to the hub, whereas spiral-spoke configurations may be arranged in a single row or in two rows (as in this work) with axial and circumferential offset. In the tweel architecture there are thin radial spoke-like members connecting the outer ring to the inner hub, whereas in the twin architecture the reinforcing elements consist of multiple curved and interconnected members arranged in a denser and more layered configuration.

For this initial analysis, the design parameters are set to the values reported in Tab.4.9.

Parameter	**Symbol**	**Value**
Outer radius	R_{ext}	0.5 m
Inner radius	R_{int}	0.25 m
Wheel width	B	0.4 m
Outer ring thickness	t_{ext}	0.003 m
Inner ring thickness	t_{int}	0.003 m
Reinforcement thickness	t_{rinf}	0.003 m
Number of wheels	N	8
Vehicle mass	M	7000 kg
Number of reinforcing elements	N_{elem}	9

Table 4.9: Initialization values adopted for the FEM parametric loop.

Outer radius, width and load per wheel are defined through the analytical analysis, while the other parameters are initialized following other criteria.
The inner radius is defined according to the specifications of the electric motor. In the case of the Twin carcass architecture, the radius is much greater than 220 mm due to the geometric and structural characteristics of the reinforcing elements. Indeed, the reinforcements are shaped as semicircles with a radius equal to the distance between the inner ring and the outer ring.

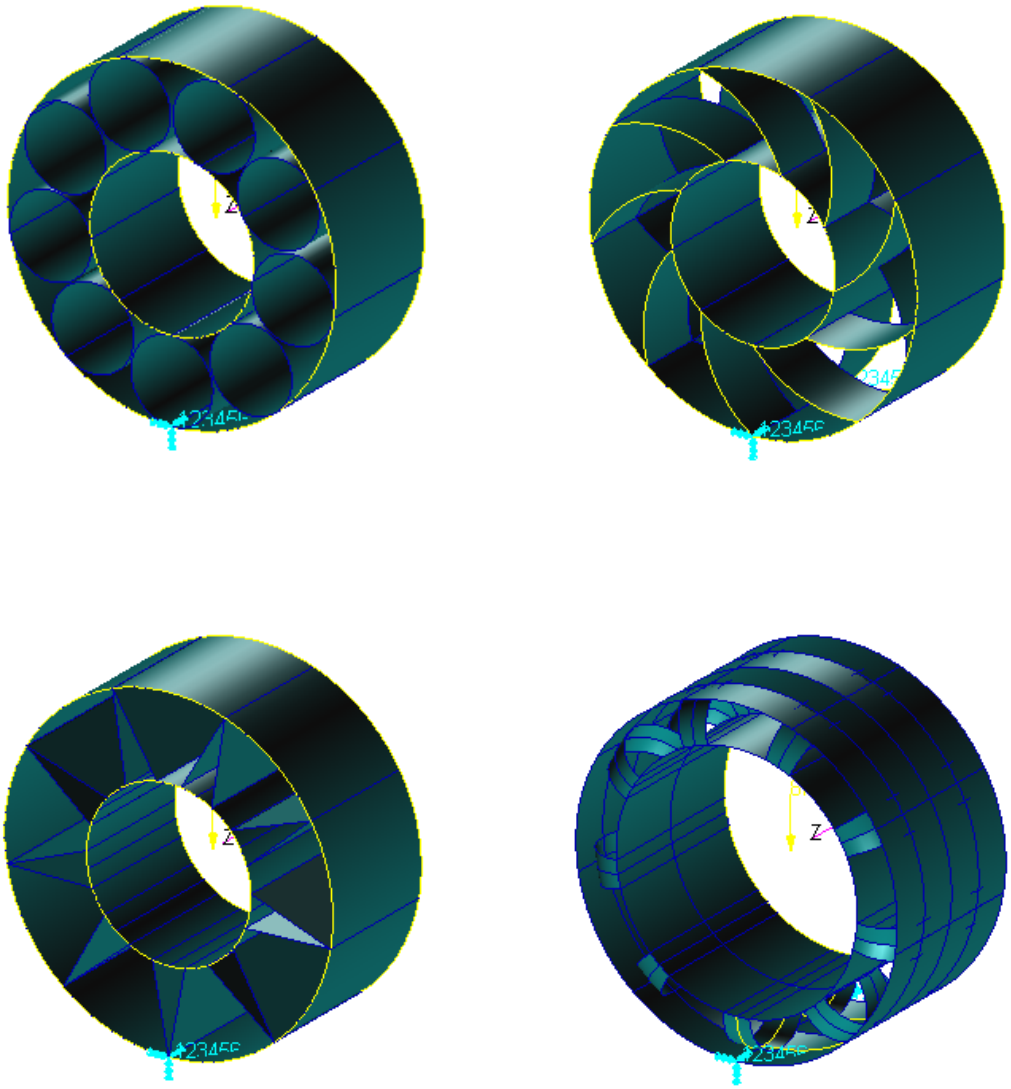

Figure 4.21: Wheel architectures in the numerical analysis. Top left: Hoop architecture; Top right: Spiral architecture; Bottom left: Tweel architecture; Bottom right: Twin architecture

The number of reinforcements is selected by considering the worst-case scenario from a weight standpoint, namely the maximum number of reinforcing elements that can be accommodated without geometric interference or overlap.

Thickness selection is based on the stiffness requirement and available sheet size (from 1 to 5 mm) [19]. For this preliminary sizing of the cylindrical wheel, shell, hub and reinforcement thicknesses are all selected equal to 3 mm. Considering the wheel size and the lightweight aluminum design target, values of about 2–5 mm are consistent with thin-walled stiffened structures (while remaining compatible with manufacturing constraints).
A sensitivity study is subsequently carried out in order to evaluate both the effect of a uniform thickness variation for all wheel components (Subsec.4.4.2) and the optimal balance among different thickness values assigned to the various parts of the wheel (Subsec.4.4.3).

Therefore, a normalized comparison is carried out in order to identify the most suitable wheel architecture, highlighting the inherent trade-off between structural efficiency and weight reduction (Fig.4.22).

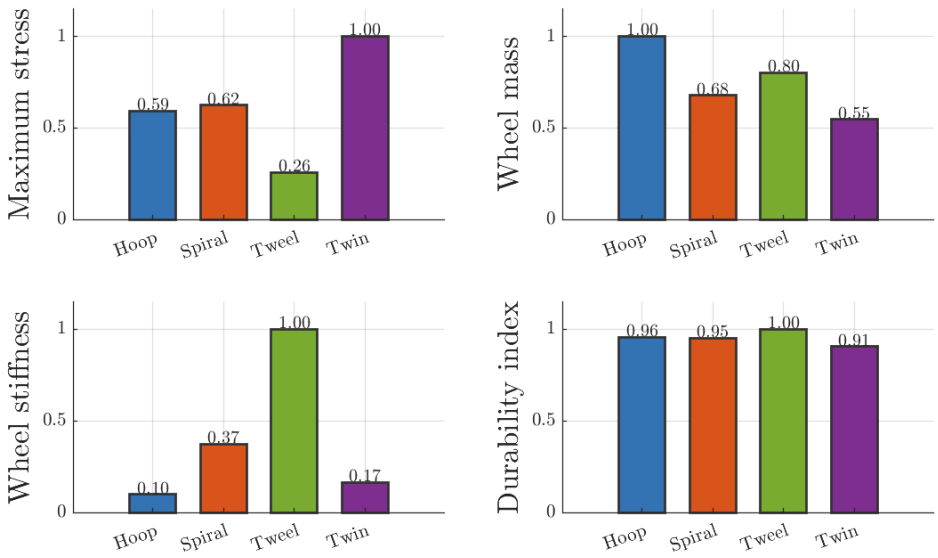

Figure 4.22: Wheel architecture comparison with values normalized with respect to the maximum

Among the four configurations, the Tweel architecture shows the most favorable mechanical behavior, as it combines the lowest maximum stress, the highest stiffness and the highest durability index. This indicates a more efficient load transfer through the internal reinforcing structure and a better overall resistance to deformation. By contrast, the Twin architecture is the lightest solution, but this advantage is associated with the highest stress level and a relatively low stiffness,

suggesting that mass reduction is achieved at the expense of structural performance. The Spiral architecture provides a more balanced response, with intermediate values in all the considered metrics, while the Hoop architecture appears mechanically less competitive mainly because of its very low stiffness, despite maintaining acceptable stress and durability levels.
In the final assessment, the Tweel and Spiral architectures emerge as the most promising solutions for this type of wheel. However, the manufacturability of all four architectures is also evaluated in order to support the final design decision.

4.4.2 Manufacturing and process selection

Alongside the structural assessment, a manufacturing-oriented analysis is also carried out in order to identify the wheel architecture that is not only mechanically efficient, but also realistically producible.

In this work, the reference manufacturing process is assumed to be metal additive manufacturing, and more specifically Laser Powder Bed Fusion (LPBF)/ Selective Laser Melting (SLM) of aluminium alloys. This choice was motivated by several factors. First, additive manufacturing enables the fabrication of geometrically complex lightweight structures that would be difficult, costly or even impossible to obtain through conventional processes. This makes it particularly suitable for non-pneumatic wheel concepts characterized by internal supporting members, curved spokes, and highly integrated geometries. In addition, additive manufacturing can reduce the total number of components, thereby simplifying assembly and increasing structural integration.
The adoption of metal additive manufacturing is also consistent with the long-term perspective of advanced and distributed production in harsh or remote environments. In particular, such technologies are increasingly regarded as promising solutions for future in-situ manufacturing scenarios in the aerospace sector, owing to their flexibility, limited tooling requirements and suitability for highly customized designs [24].

Within this manufacturing framework, AlSi10Mg is considered as an alternative to the Al7075 alloy adopted in the previous structural analyses. The reason for this choice lies in the fact that AlSi10Mg, although not mechanically equivalent to Al7075, provides partially comparable properties while being significantly more compatible with established LPBF/SLM processes. Therefore, it cannot be regarded as a direct one-to-one replacement, particularly because of its lower strength and ductility, but it remains a relevant candidate for additively manufactured components.

As shown in Table 4.10 and discussed in [25], AlSi10Mg exhibits lower density,

tensile strength, yield strength, elongation at break and hardness than Al7075, while the elastic modulus is approximately comparable for the two alloys. In addition, Al7075 shows a higher coefficient of thermal expansion, whereas AlSi10Mg exhibits higher fracture toughness. With regard to melting behaviour, AlSi10Mg has a higher minimum melting temperature, while Al7075 has a higher maximum melting temperature, resulting in a broader melting range for the latter.
For these reasons, AlSi10Mg may be regarded as a manufacturable and technically viable solution for additively manufactured lunar rover wheels. Nevertheless, because lunar regolith is highly abrasive, particular attention should also be paid to wear protection and suitable surface treatments or protective coatings should be considered for the most exposed regions of the wheel.

In the present study, AlSi10Mg is modeled as an isotropic linear-elastic material for the sake of simplicity and to ensure a consistent comparison among the different wheel architectures. However, it should be noted that LPBF-manufactured AlSi10Mg may exhibit anisotropic mechanical behavior due to build orientation and process-induced microstructural heterogeneity.

Property	**Al7075**	**AlSi10Mg**
Density [kg/m^3]	2810	2680
Ultimate tensile strength [MPa]	572.3	442.0
Yield strength [MPa]	503.3	264.0
Tensile modulus [GPa]	71.7	71.0
Elongation at break [%]	11	9
Fracture toughness [MPa$\sqrt{\text{m}}$]	20.0–29.0	58.0
Brinell hardness [HB]	150	119
Thermal expansion coefficient [10^{-6}/K]	23.58–25.20	20.23–21.24
Melting range [°C]	476.7–635.0	570.0–590.0

Table 4.10: Properties comparison of Al7075 and AlSi10Mg for structural and additive-manufacturing considerations

Based on these considerations, the manufacturability comparison is developed according to a Design for Additive Manufacturing (DfAM) approach. Rather than evaluating the architectures only in terms of geometric simplicity, the analysis accounted for the main constraints typically associated with AM processing, namely build orientation, support generation and removal, powder evacuation, accessibility for post-processing, sensitivity to distortion and residual stresses and relative production cost [26]. These aspects are particularly relevant in the case of wheel-like structures with enclosed or semi-enclosed internal regions, where the geometric freedom offered by additive manufacturing must be balanced against practical

fabrication limitations.

A semi-quantitative scoring procedure is, therefore, introduced, assigning values (from 1 to 5) to five manufacturing criteria: *geometric complexity*, *ease of production*, *ease of post-processing/assembly*, *tolerance robustness* and *estimated cost*. The final manufacturing score is obtained as a weighted sum of these contributions, so as to capture the overall balance between printability, process robustness and expected production effort.

This methodology makes it possible to compare the proposed wheel architectures through a structured and reproducible framework, consistent with the current DfAM literature for metal AM. In this way, the final selection is not based solely on structural performance, but on a broader engineering compromise between mechanical behavior and manufacturability.

Geometric complexity - Ease of production - Ease of post-processing

A first qualitative manufacturing screening is performed directly from the wheel geometries by considering geometric complexity, ease of production and ease of post-processing. The purpose of this preliminary step is not to provide a definitive manufacturing ranking, but rather to identify the architectures that appear more suitable for metal additive manufacturing on the basis of their structural layout.

From a geometric point of view, the *Hoop* architecture shows a regular and repetitive internal arrangement, which makes its geometry easier to interpret and potentially easier to control during manufacturing. The *Spiral* architecture is more complex, since the curved reinforcing members generate a less straightforward internal layout. The *Tweel* architecture, despite the presence of several slender internal spokes, remains visually open and well organized, whereas the *Twin* architecture exhibits the highest geometric complexity due to its denser and more intricate internal configuration.

With regard to ease of production, the *Tweel* architecture appears to be the most favorable solution, mainly because its open spoke-like structure seems more compatible with a clear build strategy and with a reduced obstruction of the internal volume. The *Hoop* configuration also appears relatively favorable, thanks to its regular geometry, although the curved internal members may still introduce some manufacturing constraints depending on the selected build orientation. The *Spiral* architecture represents an intermediate case, as the curvature of its reinforcing elements may lead to less straightforward printing conditions. By contrast, the *Twin* architecture appears to be, once again, the least favorable, since its denser

internal layout is expected to complicate the build process and increase manufacturing difficulty.

A similar trend is observed for ease of post-processing. The more open geometries of the *Tweel* and, to a slightly lesser extent, the *Hoop* architecture suggest better accessibility for support removal, powder evacuation and visual inspection of the internal structure. The *Spiral* architecture is again intermediate, as its curved members may partially reduce accessibility to some regions. The *Twin* architecture appears the most critical, because its more compact and layered internal arrangement is expected to hinder access to the inner zones and therefore make post-processing operations more difficult.

Tolerance robustness

The tolerance robustness criterion is introduced in order to evaluate how sensitive each wheel architecture is to small variations in the thickness of its structural components. This aspect is particularly relevant in the context of metal additive manufacturing, where deviations from nominal dimensions may arise because of process-related effects, such as local distortion, thermal shrinkage or limited dimensional accuracy. In this work, tolerance robustness is assessed through a sensitivity analysis in which one thickness parameter at a time is varied around its nominal value ($\pm 5\%$ / $\pm 10\%$), while the remaining geometric parameters are kept constant. For each variation, the resulting changes in maximum stress, wheel stiffness and durability index are evaluated with respect to the reference configuration. In this way, the robustness of each architecture is quantified by observing how strongly its structural response changes under small geometric perturbations: the smaller the variation in the output quantities, the higher the tolerance robustness of the corresponding wheel configuration.

The tolerance robustness analysis of the Hoop architecture (Fig. 4.23) shows a limited sensitivity with respect to variations in the outer and inner ring thicknesses, as the corresponding changes in maximum stress, wheel stiffness and durability index remain relatively moderate and regular. This suggests that the global structural response is only weakly affected by small dimensional perturbations of the ring components.
A significantly stronger sensitivity is instead observed for the reinforcement thickness. In this case, positive thickness variations lead to a marked increase in maximum stress, accompanied by a rise in stiffness and a reduction in durability index. Therefore, the results indicate that the tolerance robustness of the Hoop configuration is mainly governed by the reinforcing elements, whereas the outer and inner rings play a less critical role. Therefore, from both a design and manufacturing

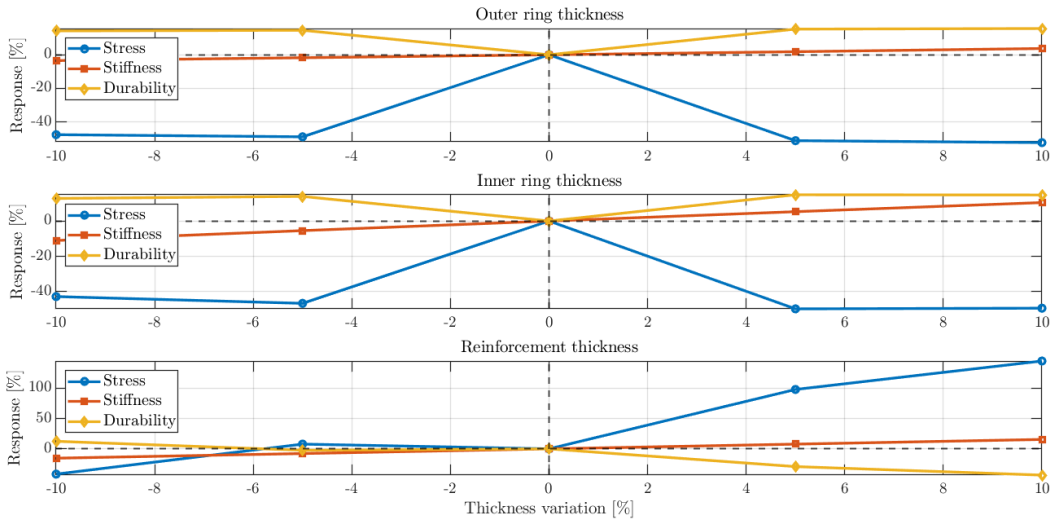

Figure 4.23: Tolerance robustness of the Hoop architecture under independent thickness variations of the outer ring, inner ring, and reinforcing elements, expressed in terms of percentage changes in maximum stress, wheel stiffness, and durability index with respect to the nominal configuration.

perspective, particular attention should be paid to the dimensional control of the reinforcements.

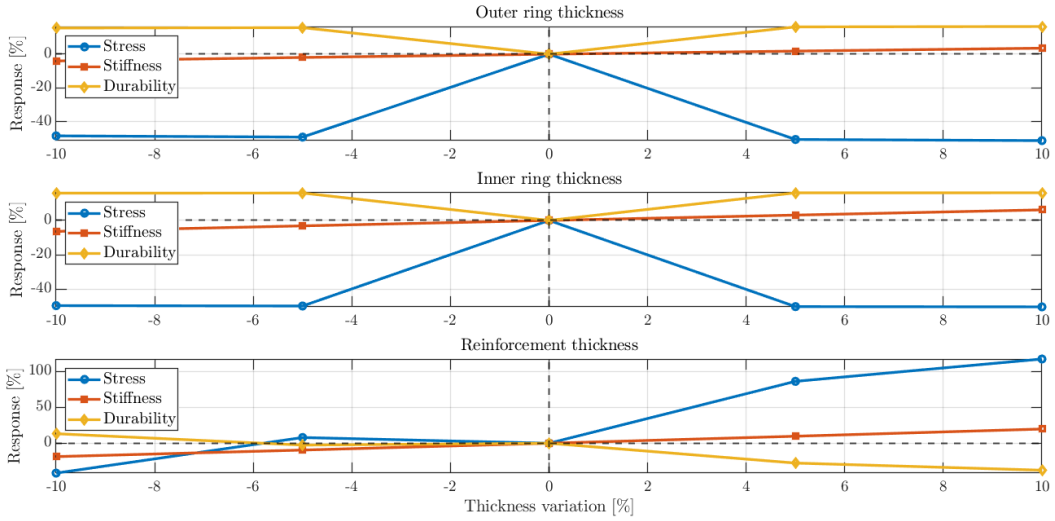

Figure 4.24: Tolerance robustness of the Spiral architecture

The Spiral architecture (Fig. 4.24) shows a sensitivity pattern that is broadly

similar to the Hoop configuration, but with a slightly more pronounced effect of thickness variations on stiffness and durability. The outer and inner ring thicknesses have a limited influence on the global response, whereas the reinforcement thickness remains the dominant parameter. In particular, the stress response is strongly affected by variations in the reinforcing elements, confirming that the internal curved members govern the structural robustness of this configuration.

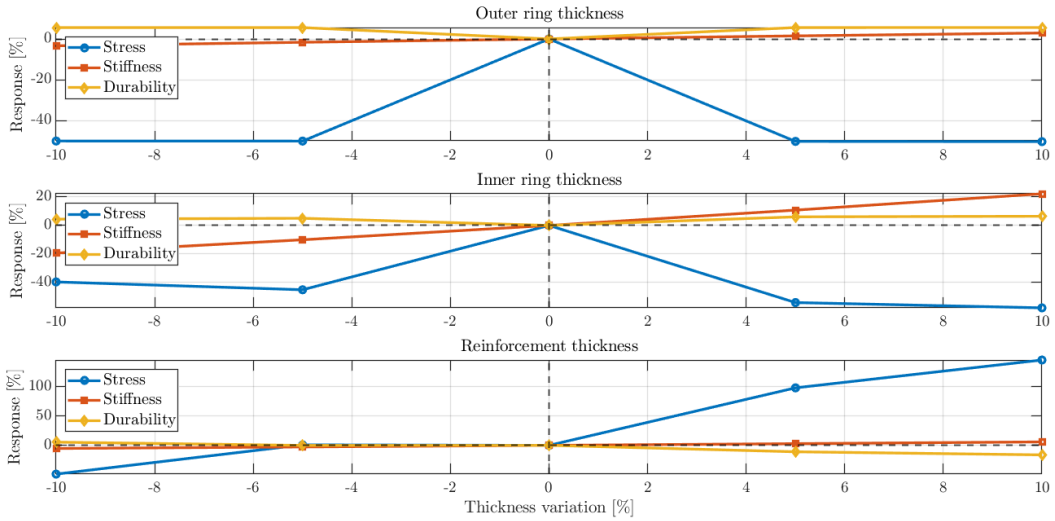

Figure 4.25: Tolerance robustness of the Tweel architecture

The Tweel architecture (Fig. 4.25) exhibits a comparatively stable response with respect to variations in the ring thicknesses, while the reinforcement thickness again plays the most relevant role. In this case, the sensitivity of stress to reinforcement perturbations is particularly evident, whereas the durability index remains less affected than in the other architectures. This suggests that the structural behavior of the Tweel configuration is mainly controlled by the spoke-like internal members, which represent the key design feature from a robustness standpoint.

The Twin carcasses (Fig. 4.26) architecture appears to be the most sensitive configuration overall, especially with respect to variations in the reinforcement thickness.

Based on the comparison of the robustness scores, the *Tweel* architecture is identified as the most robust configuration, followed by the *Spiral* and *Hoop* solutions, while the *Twin* architecture shows the lowest robustness.

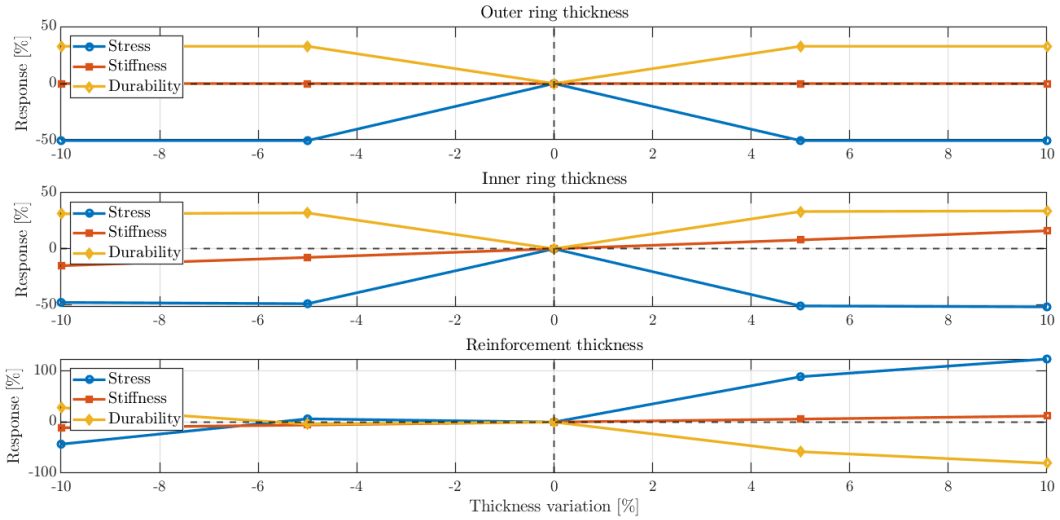

Figure 4.26: Tolerance robustness of the Twin carcasses architecture

Manufacturing costs

The estimated manufacturing cost is approximated through a simplified mass-based metric, computed on the baseline configuration (Fig.4.22). Under this assumption, lighter solutions are considered economically preferable and are assigned a higher estimated-cost score.
Overall, the *Twin* architecture appears as the most economical solution (lowest index), followed by the *Spiral* and *Tweel* configurations, while the *Hoop* architecture shows the highest estimated cost (maximum normalized mass).

Final manufacturing evaluation

The final evaluation of the manufacturing process of the four wheel architectures is done by assigning a score from 1 to 5 to each of the selected criteria, namely geometric complexity, ease of production, ease of post-processing, tolerance robustness and estimated cost. The Tab.4.11 provides a synthetic comparison of the different configurations and highlights their relative strengths and weaknesses from a manufacturability perspective.

In Fig.4.27, the final manufacturing ranking is identified. Overall, the results indicate that the *Tweel* architecture provides the best balance among geometric complexity, producibility, post-processing, robustness and estimated cost, followed by the *Spiral* and *Hoop*. The *Twin* architecture appears to be the least appropriate from a manufacturing perspective.

Type	Geometric complexity	Ease of production	Ease of post-processing	Tolerance robustness	Cost
Hoop	4	4	4	3	2
Spiral	3	3	3	4	4
Tweel	4	5	5	5	3
Twin	2	2	2	2	5

Table 4.11: Manufacturing-oriented scoring (1–5, where 5 indicates the most favorable outcome) for the four wheel architectures.

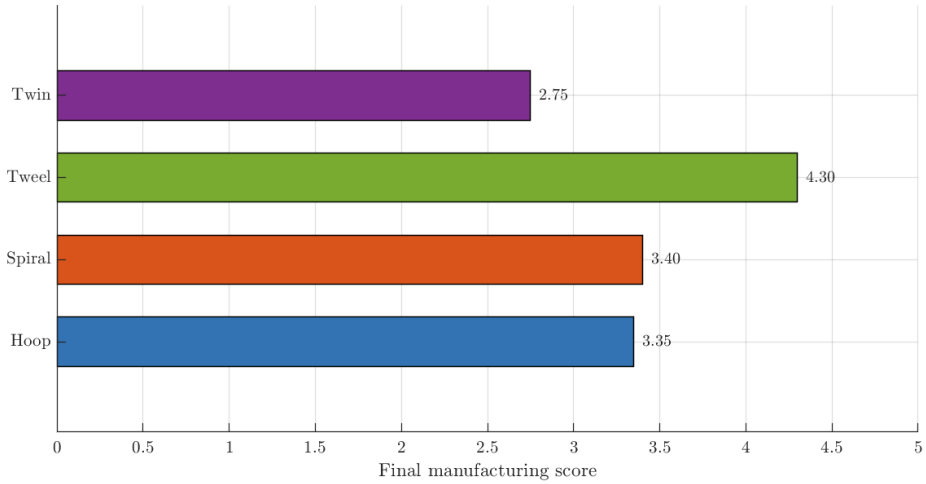

Figure 4.27: Comparison of the final manufacturing scores for the analyzed wheel concepts.

By combining the manufacturability assessment with the structural performance results, the *Tweel* architecture emerges as the most suitable solution among the analyzed wheel concepts.

4.4.3 Architectural parametric study

A more detailed investigation is carried out on the internal geometry of the selected wheel architecture. The aim is to identify the final wheel structure that is best suited to the rover locomotion system considered in this study. In particular, the architecture is analyzed in greater detail in order to assess the influence of the reinforcing elements and thickness parameters on the overall structural response.

A parametric study is carried out on 108 configurations obtained by varying the

outer skin thickness, inner skin thickness, reinforcement thickness and number of spokes. The reinforcement thickness is varied within the range $t_{\text{rinf}} \in [\,2,\,3\,]$ mm; the internal end external thickness is varied within the range $t_{\text{rinf}} \in [\,1,\,2\,]$ mm; the number of reinforcements is varied within the interval $N_{\text{rinf}} \in [\,6,\,9\,]$. These limits are defined in order to explore structurally meaningful configurations while excluding solutions that are either too flexible to provide an effective stiffening contribution or excessively heavy and geometrically crowded, as also described in [19].

For each configuration, a static finite element analysis is performed in Patran/Nastran and the main structural response quantities are extracted, namely maximum stress, vertical deflection, wheel mass, stiffness and durability index. The simulation results are then post-processed in MATLAB in order to compare the candidate designs on a consistent basis. First, non-admissible or erroneous configurations are removed from the dataset. Then, the remaining solutions are filtered according to the prescribed design constraints and ranked through a multi-objective procedure based on normalized performance indicators. In parallel, the Pareto front is identified to highlight the non-dominated solutions, i.e. the configurations for which no objective can be improved without worsening at least one of the others.

The obtained results show a clear trade-off between structural performance and mass. In general, lighter configurations tend to exhibit larger deflections and, in several cases, higher stress levels, whereas heavier solutions provide improved stiffness and lower deformation, at the expense of increased mass. The Pareto front confirms that no single configuration is optimal in an absolute sense; rather, a set of efficient designs exists, each representing a different compromise between weight, stress and deflection. Within this set, the most promising solutions are those capable of limiting both stress and deformation without a significant mass penalty. This preliminary screening therefore allowed the design space to be reduced to a limited number of meaningful candidates, which are subsequently selected for further numerical assessment.

Among the admissible solutions, three configurations are selected, in Tab. 4.12, as the most representative for the final convergence and validation analyses: Design 64, Design 90 and Design 13. Design 64 corresponds to the best overall configuration, i.e. the admissible design with the lowest (and best) global score obtained from the weighted multi-objective ranking. Design 90 is selected as the most critical admissible configuration, namely the solution closest to the design limits in terms of structural response and therefore particularly relevant for assessing the robustness of the numerical results. Design 13, instead, is identified as the lightest admissible configuration among the remaining candidates, and is therefore significant from

a mass-efficiency perspective. These three cases are consequently adopted for the mesh convergence study, since they represent three complementary design conditions: the best global compromise, the most critical feasible solution and the lightest feasible design.

Case	**ID**	R_{ext} [m]	R_{int} [m]	W [m]	t_{ext} [m]	t_{int} [m]	t_{rinf} [m]	N_{rinf} [-]
Best overall	64	0.50	0.25	0.40	0.0015	0.0020	0.0020	9
Most critical	90	0.50	0.25	0.40	0.0020	0.0015	0.0025	7
Lightest feasible	13	0.50	0.25	0.40	0.0010	0.0015	0.0020	6

Table 4.12: Selected wheel configurations adopted for the subsequent mesh convergence study.

The admissible design space is illustrated in the 3D objective plot , where the solutions are distributed as a function of mass, deflection+ and stress, while the color scale reflects the global score. The Pareto-front plot provides a complementary representation by identifying the non-dominated configurations in the stress–deflection plane, thus highlighting the most efficient design trade-offs (Fig. 4.28).

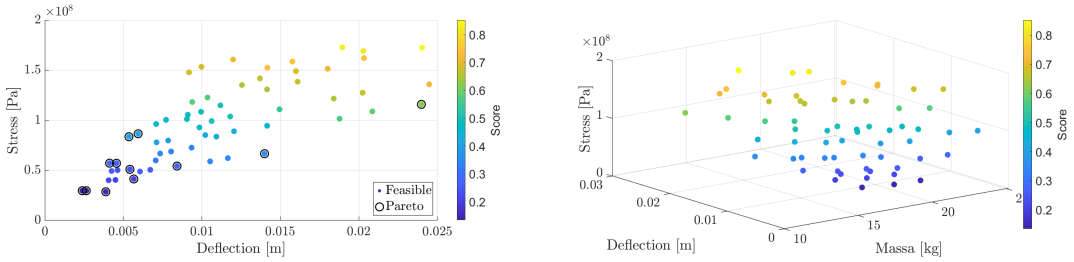

Figure 4.28: On the left: Pareto front - Deflection versus Stresses ; on the right: Admissible design space 3D

Convergence analysis

A mesh convergence analysis is performed in order to assess the sensitivity of the numerical results to the discretization adopted in the finite element model. This verification step is required to ensure that the structural quantities used in the design comparison are not affected by an excessively coarse mesh and can therefore be considered representative of the actual mechanical response of the wheel. The analysis is carried out on the three configurations selected from the

preliminary multi-objective screening, namely the best overall design, the most critical admissible case and the lightest admissible configuration. For each case, the geometry, material properties, loading conditions and boundary conditions are kept unchanged, while only the mesh size is varied: *mesh global length* $\in [0.04, 0.01]$ (Fig. 4.29).

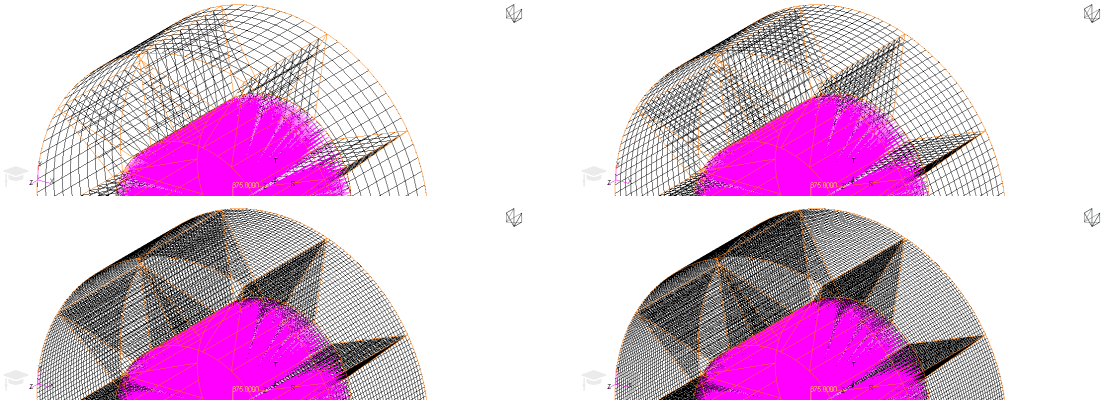

Figure 4.29: Mesh configurations adopted for the convergence analysis. Top left: 0.04; top right: 0.025; bottom left: 0.0125; top right: 0.01.

The convergence study is evaluated by monitoring the evolution of the two main response quantities, namely vertical deflection and maximum stress, as a function of the mesh global edge length. As shown in Fig. 4.30, the displacement response tends to stabilize for the finer discretizations, whereas the coarsest mesh leads to a significant deviation, particularly for Case 1 . A similar trend is observed for the stresses, where the response obtained with the coarsest mesh is very different from that associated with the finer meshes, again with the strongest sensitivity observed for Case 1.

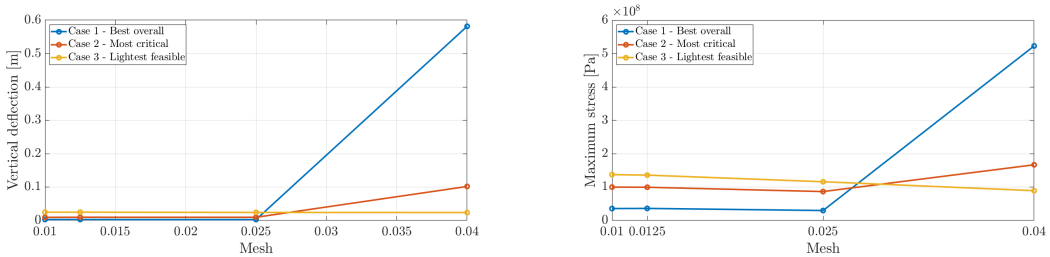

Figure 4.30: Convergence analysis. On the left: Deflection versus length of the mesh ; on the right: Stresses versus length of the mesh

Overall, the convergence analysis shows that the coarsest mesh is not adequate for

a reliable structural assessment, since it introduces a substantial overestimation of both deflection and stress in the most sensitive configurations. On the other hand, the finer meshes provide mutually consistent results and can therefore be considered sufficiently accurate for the analyses. The observed behavior is fully consistent with the expected response of thin-walled reinforced structures, for which coarse discretizations may fail to capture local stiffness and stress distributions with sufficient fidelity.

Final wheel architecture

Based on the preliminary parametric analysis, the multi-objective ranking procedure and the subsequent mesh convergence assessment, the best-performing configuration is selected as the final wheel architecture for the present study (See Tab. 4.12 : Best overall). More specifically, this configuration emerged as the most effective compromise among structural performance and mass, while also satisfying the imposed admissibility criteria in terms of stress and vertical deflection. The convergence analysis further confirmed that the corresponding numerical results are sufficiently stable with respect to mesh refinement, thus supporting the reliability of the selected solution.

It should be noted that this selection is valid within the scope of the present work, which is limited to static finite element analyses. Therefore, the identified architecture should be regarded as the optimal solution among the analyzed configurations under the adopted loading and modeling assumptions, rather than as an absolute optimum in a broader sense. Nevertheless, the selected design can be considered as a suitable reference configuration for the pressurized rover wheel, since it provides a balanced combination of performance characteristics, structural stiffness, stress control and mass efficiency.

The stress and displacement contour plots of the final configuration are reported in Fig.4.31, 4.32. The displacement field highlights the global deformation pattern of the wheel under the applied load, whereas the stress field allows the most critical regions of the structure to be identified.

The largest displacement is mainly located along the outer rim and in the sectors between adjacent reinforcements, whereas the central hub region remains comparatively stiffer due to the structural support provided by the inner layout. This behavior confirms that the reinforcement arrangement effectively contributes to load redistribution and to the overall control of the wheel deformation.

The stress contour, on the other hand, exhibits a more localized response. The

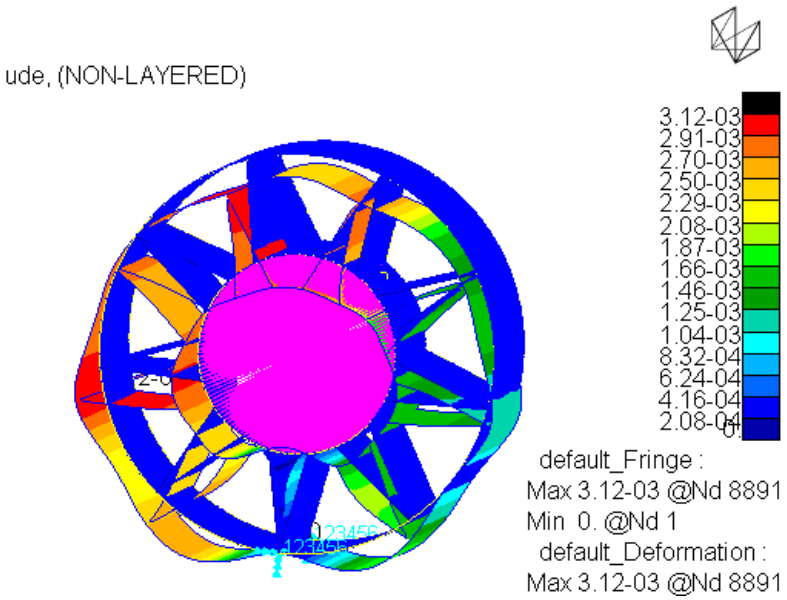

Figure 4.31: Contour plot of the total deformation distribution in the tweel wheel model.

highest stress levels are concentrated in the connection regions between reinforcements, hub and outer rim, namely where the load path is combined with geometric and stiffness discontinuities. Most of the wheel structure is instead characterized by lower stress values, indicating a generally regular structural behavior. The identified high-stress regions therefore represent the critical areas of the design and should be considered with particular attention in future developments, such as fatigue verification or local geometric refinement.

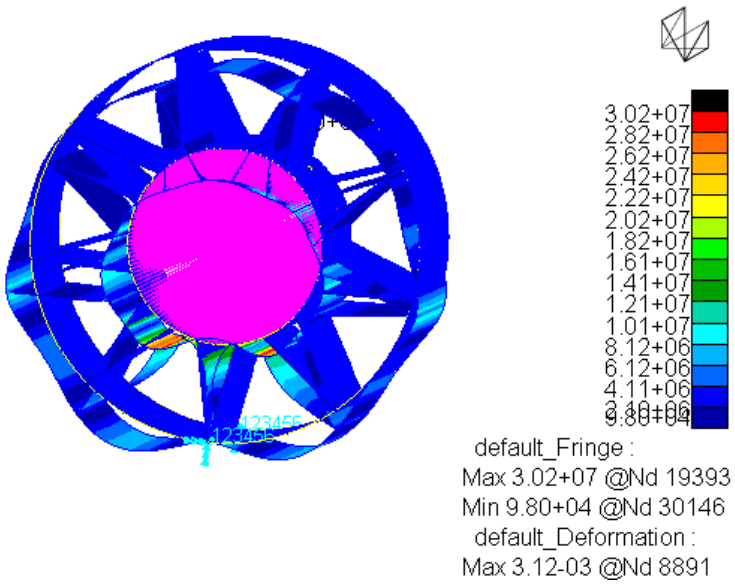

Figure 4.32: Contour plot of the stress distribution in the tweel wheel model.

Chapter 5

Conclusions and future works

5.1 Conclusions

This thesis addressed the preliminary design of an advanced traction system for a pressurized lunar rover, with specific focus on the wheel as the key element governing mobility on deformable regolith. The work was motivated by the need to identify a wheel solution capable of combining adequate traction capability, limited sinkage, low power demand and reduced structural mass, while remaining compatible with the severe environmental and operational constraints imposed by long-range lunar surface exploration.

A major contribution of the thesis lies in the development of an integrated parametric design framework in which terramechanics-based mobility analysis and preliminary structural sizing are combined within a single workflow. Starting from classical wheel–soil interaction theories, the study reformulated the problem in a form suitable for rapid preliminary design and comparative assessment of a large number of candidate solutions. In this context, two closed-form approximation strategies are investigated, namely a constant stress approximation and a quadratic stress approximation, in order to overcome the computational burden of directly evaluating the full stress distributions along the contact patch.
The obtained results showed that the simplified constant-stress formulation, although useful for fast estimates, tends to underestimate wheel performance and is therefore less suitable when a realistic ranking of candidate solutions is required. By contrast, the quadratic approximation proved more consistent with the expected nonlinear stress evolution along the wheel–soil interface, providing a more reliable basis for the evaluation of drawbar pull, motion resistance, torque and

power demand. The analysis also confirmed the beneficial role of wheel compliance: compared with rigid wheels, flexible configurations increase the effective contact area, reduce ground pressure and generally improve mobility performance on soft regolith.
The sensitivity analysis highlighted the strong influence of a limited number of design variables on the overall system response. In particular, wheel diameter and width were confirmed to be primary drivers of sinkage, contact pressure and traction capability, while slip ratio plays a central role in determining the balance between useful traction and energetic losses. The number of wheels also emerged as an important architectural parameter because of its effect on load distribution and, consequently, on wheel–terrain interaction. These trends allowed the identification of a consistent set of design guidelines for pressurized lunar rovers operating on highly deformable terrain.
On the basis of the analytical trade-off, a reference cylindrical configuration is selected and used as the baseline for further structural assessment. This phase made it possible to derive representative values for contact quantities, stress levels, torque demand and drive power, thereby establishing a coherent link between trafficability requirements and drivetrain integration. In particular, the wheel-side requirements confirmed that the traction subsystem must be designed together with the hub, reduction stage, and actuator architecture, rather than as an isolated rolling element.

A further relevant outcome of the thesis is the comparison among four non-pneumatic wheel concepts: hoop spring, modified spiral spring, tweel, and twin-carcasses architectures. Their structural response and manufacturability are assessed through finite element analyses and manufacturing-oriented criteria. Among the analyzed concepts, the tweel architecture emerges as the most promising solution, as it provides the best balance between structural efficiency, stiffness, durability, robustness to dimensional variations and producibility. This result is particularly significant because it supports the idea that future lunar pressurized rovers will likely benefit from highly integrated compliant wheel architectures, in which the internal reinforcing members play a dominant role in both load transfer and global performance.

Overall, the thesis demonstrates that the design of lunar rover wheels cannot be reduced to a purely geometric or structural problem. Instead, it requires a multi-disciplinary approach in which terramechanics, structural mechanics, drivetrain requirements and manufacturing aspects are considered simultaneously. In this sense, the proposed methodology represents a useful design tool for the preliminary synthesis and ranking of wheel concepts for future planetary mobility systems.

At the same time, the present work should be interpreted as a preliminary design

study rather than a fully validated final design. The adopted models rely on simplifying assumptions, including homogeneous regolith properties, quasi-static operation, simplified contact geometries and static structural analyses. Nevertheless, these limitations do not reduce the value of the work; rather, they define a clear and solid starting point for more advanced future developments. This thesis therefore provides both a coherent design methodology and a technically grounded baseline solution for the next generation of pressurized rover traction systems.

5.2 Future work

Several developments can naturally extend the present work and further improve both the fidelity of the models and the maturity of the proposed wheel concept.

- **Integration of grousers and tread features.** One of the most immediate developments concerns the introduction of grousers, lugs or other surface-texturing solutions on the outer wheel band. Their geometry, number, spacing, height, inclination and circumferential distribution could be optimized in order to increase drawbar pull, reduce slip, improve obstacle negotiation and enhance traction on loose regolith.

- **Buckling and local instability analyses.** Since the selected non-pneumatic architectures rely on thin shells and compliant internal members, future work should include dedicated buckling analyses. Both linear eigenvalue buckling and geometrically nonlinear post-buckling analyses would be useful to assess the stability of the outer ring, spokes and reinforcement elements under combined radial, tangential and lateral loads. This aspect is particularly relevant for lightweight designs obtained through thin-walled metallic structures.

- **Fatigue and durability assessment under cyclic loading.** The current study mainly considered static or quasi-static structural conditions. A more realistic qualification of the wheel requires fatigue analyses under repeated loading cycles representative of long lunar traverses. This includes the accumulation of damage due to repeated wheel deformation, terrain irregularities, steering maneuvers and transient overloads induced by rock impacts and obstacle crossing.

- **Coupled wheel–suspension–actuation design.** In the present thesis, the focus is intentionally restricted to the traction element. A natural extension is therefore the integration of the wheel model with the suspension system, the steering mechanism and the propulsion chain. Such a system-level approach would allow the investigation of how wheel stiffness, suspension compliance

and actuator torque capabilities interact in determining rover ride quality, load redistribution, stability and mobility efficiency.

- **Wheel–terrain interaction under transient and non-uniform conditions.** The current terramechanics formulation assumes homogeneous terrain and quasi-static behavior. Future work should include variable soil parameters, layered regolith, local compaction effects, slopes, crater rims, trenches and rock–wheel interactions. This would make it possible to assess the robustness of the selected design under spatially varying terrain properties and more realistic operational scenarios.

- **Experimental validation with lunar regolith simulants.** The analytical and numerical results should be validated through experiments performed on representative simulants. Bevameter tests, single-wheel test rigs, sinkage tests, traction tests and obstacle-crossing experiments would provide valuable data for calibrating the terramechanics parameters and validating the predicted trends in drawbar pull, resistance and sinkage.

- **Exploration of alternative wheel architectures.** Beyond the four concepts studied here, additional wheel topologies should be considered. These may include hybrid architectures derived from the current tweel, hoop and spiral concepts, lattice-based wheels, compliant cellular structures, segmented rings or architectures with locally variable stiffness. The present framework could be used to generate and compare such new concepts systematically.

- **Material exploration.** The current study focused on aluminum-based solutions. Future work should investigate alternative materials such as titanium alloys, high-strength steels, superelastic alloys, metallic lattice materials and possibly hybrid metal–composite solutions.

- **Manufacturing process diversification.** Although LPBF/SLM additive manufacturing appears promising, other manufacturing routes should also be investigated, including conventional forming and assembly, machining plus joining, wire-based additive processes or hybrid manufacturing chains.

- **System-level optimization of the entire locomotion subsystem.** A further step would be the development of a multidisciplinary optimization framework in which wheel geometry, architecture, suspension parameters, actuator sizing, transmission ratio and control strategy are optimized simultaneously with respect to mass, power, mobility, robustness and manufacturability.

In summary, the present thesis provides a solid preliminary design basis, while the developments, outlined above, identify a clear path toward a more complete,

experimentally validated and system-integrated wheel design for future pressurized planetary rovers.

Acknowledgements

Desidero esprimere la mia sincera gratitudine al mio relatore A. Pagani e correlatori G. Palaia e K. Abu Salem per la loro guida e per la loro costante disponibilità durante tutto il percorso di tesi.

Sono profondamente grata alla mia famiglia, a mia madre Mina, a mio padre Alberto e a mio fratello Stefano, per il loro sostegno costante, l'incoraggiamento e la fiducia con cui mi hanno sempre accompagnata. Un ringraziamento speciale va al mio ragazzo Pietro, per essermi stato vicino ogni giorno, per l'aiuto e la cura con cui ha saputo sostenermi anche nei momenti più difficili.

Un pensiero affettuoso va anche ai miei amici, a quelli vicini e a quelli lontani, a quelli che fanno parte della mia vita da sempre e a quelli incontrati lungo il percorso. Un ringraziamento speciale lo dedico a Betta per aver condiviso davvero ogni momento ed esserci sempre stata dal primo giorno e ad Elena per la costante vicinanza, pur nella distanza. Tutti, ciascuno a modo proprio, mi hanno accompagnata con affetto, presenza e sostegno, rendendo questo percorso più leggero, più bello e più ricco di significato. Ringrazio ancora Francesca, Andrea, Chiara, Federico, Carlo, Giulio e Gaia per i momenti di svago, spensieratezza e complicità condivisi.

Infine, desidero ringraziare i miei colleghi, e ormai amici, sia quelli che hanno vissuto insieme a me questo stesso percorso di studi sia quelli che hanno condiviso questa esperienza di tesi, per il loro supporto, lo scambio di idee e la compagnia lungo il cammino ed in particolare Angelo, Simone, Bruna, Sara, Alessandra, Ferdinando e Alessio.

Lavorare a questa tesi mi ha ricordato che il progresso, proprio come la progettazione ingegneristica, non è mai immediato: è un processo di affinamento, adattamento e integrazione, in cui ogni miglioramento avvicina il sistema alla sua configurazione più efficace. In un certo senso, cresciamo allo stesso modo, diventando nel tempo più forti, più consapevoli e più completi, spinti non solo dalla nostra determinazione, ma anche dal sostegno di chi ci sta accanto. E forse questa è la lezione ingegneristica più rassicurante di tutte: anche il viaggio più ambizioso in avanti dipende dalla giusta trazione. Con questo spirito, guardo ora al futuro, pronta ad affrontare

la prossima sfida e il cammino che mi attende, ovunque esso mi conduca, con la consapevolezza di non essere sola, ma di poter ancora contare sul sostegno delle persone che mi vogliono bene e a cui voglio bene.

Grazie davvero.

Bibliography

[1] M. Bharadwaj, V. Bulsara, D. Lokan, S. Shariff, E. Ward, and R. Zurub. *Design of a Pressurized Lunar Rover*. Tech. rep. NASA-CR-192033. Final Report, Senior Design Project, USRA/NASA/VPI&SU. Washington, DC: NASA, Apr. 1992 (cit. on p. 4).

[2] Z. Q. Li and L. K. Bingham. *Terramechanics for LTV Modeling and Simulation*. Tech. rep. NASA White Paper. NASA, 2009 (cit. on pp. 6, 13, 16, 26, 30).

[3] V. Asnani, D. Delap, and C. Creager. *The Development of Wheels for the Lunar Roving Vehicle*. Tech. rep. NASA/TM-2009-215798. Cleveland, OH: NASA Glenn Research Center, 2009 (cit. on p. 6).

[4] C. Falchi. «Sistemi di presa e movimentazione di robot non convenzionali». Ph.D. thesis, Dottorato di Ricerca in Progettazione Meccanica. PhD thesis. Università degli Studi di Cagliari, 2011 (cit. on pp. 6, 8).

[5] V. Asnani, D. Delap, and C. Creager. *The Development of Wheels for the Lunar Roving Vehicle*. NASA Technical Memorandum NASA/TM-2009-215798. Cleveland, Ohio: National Aeronautics and Space Administration, Glenn Research Center, Dec. 2009 (cit. on p. 8).

[6] F. Maltinti. *Cenni di Meccanica della Locomozione*. Lecture notes. Corso di Costruzione di Strade, Ferrovie ed Aeroporti. 2011 (cit. on p. 12).

[7] H. Suzuki. «Terramechanics-based Analysis of Wheel Locomotion: Proposal of Field Modeling Method and Extended Terramechanics Models». PhD Thesis. Yokohama, Japan: Yokohama National University, Mar. 2021 (cit. on pp. 14, 17, 32).

[8] A. Schepanik, C. M. Gregory, M. F. Proctor, K. A. Johnson, and J. E. Breckenridge. *An Overview of Tire-Ground Contact Modeling Approaches for Surface Mobility Applications*. NASA Technical Memorandum NASA/TM–20250006958. United States: National Aeronautics and Space Administration, July 2025 (cit. on p. 14).

[9] E. Koutras, F. Moretti Leila, A. Ribaric, and S. Natsiavas. «A New Contact and Road Model for Multi-Body Dynamics Simulation of Wheeled Vehicles on Soft-Soil Terrain». In: *Research Square* (2023). Preprint. DOI: 10.21203/rs.3.rs-3611606/v1 (cit. on pp. 15, 25, 32).

[10] C. Senatore. «Prediction of Mobility, Handling, and Tractive Efficiency of Wheeled Off-Road Vehicles». PhD thesis. Blacksburg, VA, USA: Virginia Polytechnic Institute and State University, 2010 (cit. on pp. 15, 22, 25).

[11] B. Kirupanand, T. R. Gallang, T. Kowsik, M. M. K. J. Kumar, R. Thushan, and S. C. Premanline. «Automated Solution for Effective Town Planning». In: *IEEE International Conference on Advances in Engineering, Science and Management (ICAESM)*. Nagapattinam, India: IEEE, 2012, pp. 1–6 (cit. on p. 15).

[12] K. Terzaghi. *Theoretical Soil Mechanics*. New York: John Wiley & Sons, 1943 (cit. on p. 16).

[13] A. Sheehan, C. M. Swezey, M. P. Proctor, K. A. Johnson, and J. B. Breckenridge. *An Overview of Tire-Ground Contact Modeling Approaches for Surface Mobility Applications*. NASA Technical Memorandum NASA/TM–20250006958. Cleveland, OH: National Aeronautics and Space Administration, July 2025 (cit. on p. 17).

[14] K. Yoshida and G. Ishigami. «Steering Characteristics of a Rigid Wheel for Exploration on Loose Soil». In: *Proceedings of the 2004 IEEE/RSJ International Conference on Intelligent Robots and Systems*. Sendai, Japan: IEEE, Sept. 2004 (cit. on pp. 23, 25).

[15] H. Schwanghart. «Lateral Forces on Steered Tyres in Loose Soil». In: *Journal of Terramechanics* 5.1 (1968), pp. 9–29 (cit. on p. 25).

[16] D. S. Apostolopoulos. «Analytical Configuration of Wheeled Robotic Locomotion». PhD thesis. Pittsburgh, PA: The Robotics Institute, Apr. 2001 (cit. on pp. 26, 28, 29).

[17] D. Cardile, N. Viola, S. Chiesa, and A. Rougier. «Applied design methodology for lunar rover elastic wheel». In: *Acta Astronautica* 81 (2012), pp. 826–838. DOI: 10.1016/j.actaastro.2012.07.008 (cit. on pp. 28, 37, 50).

[18] Z. Jian, W. Smith, and H. Peng. «Fast analytical models of wheeled locomotion in deformable terrain for mobile robots». In: *Journal of Terramechanics* 49.3-4 (2012), pp. 199–209. DOI: 10.1016/j.jterra.2012.04.002 (cit. on pp. 29, 51).

[19] G. Sharma, S. Tiwary, A. Kumar, H. N. Suresha Kumar, and K. A. K. Murthy. «Systematic design and development of a flexible wheel for low mass lunar rover». In: *Journal of Terramechanics* 76 (2018), pp. 39–52. DOI: 10.1016/j.jterra.2017.12.001 (cit. on pp. 37, 50, 65, 74).

[20] Y. Cui, G. Zheng, and M. Zhou. «Calculation and Simulation of Elastic Deformation of Thin-walled Rings». In: *Proceedings of CAD'19 (International CAD Conference)*. Singapore, June 24–26, 2019, pp. 80–85. DOI: 10.14733/cadconf.2019.80-85 (cit. on p. 50).

[21] M. I. Malenkov, V. A. Volov, and E. A. Lazarev. «Quality of the Locomotion System in Planetary Rovers». In: *Russian Engineering Research* 36.10 (2016), pp. 800–808. DOI: 10.3103/S1068798X16100129 (cit. on p. 54).

[22] Kollmorgen. *AKM2G Servo Motor*. 2026. URL: https://www.kollmorgen.com/en-us/products/motors/servo/akm-series/akm2g/akm2g-servo-motor (visited on 03/12/2026) (cit. on p. 59).

[23] Harmonic Drive. *CSG-GH Gearbox*. 2026. URL: https://www.harmonicdrive.net/products/servo-mount-gearheads/harmonic-drive/csg-gh (visited on 03/12/2026) (cit. on p. 60).

[24] M. Taghizadeh and Z. H. Zhu. «A comprehensive review on metal laser additive manufacturing in space: Modeling and perspectives». In: *Acta Astronautica* 223 (2024), ??–?? DOI: 10.1016/j.actaastro.2024.06.027 (cit. on p. 66).

[25] M. Paviolo. «Materiali per l'Additive Manufacturing: caratteristiche e procedure certificative per l'aerospazio». Tesi di laurea magistrale. Politecnico di Torino, 2021 (cit. on p. 66).

[26] E. Bianchi. *Come sfruttare le potenzialità dell'additive con il DfAM (Design for Additive Manufacturing)*. Sept. 22, 2023. URL: https://www.ilprogettistaindustriale.it/come-sfruttare-le-potenzialita-delladditive-con-il-design-for-additive-manufacturing/ (visited on 03/16/2026) (cit. on p. 67).